Journal of Medicinal Chemistry

Article

pubs.acs.org/jmc

Discovery and Mechanism Study of SIRT1 Activators that Promote the Deacetylation of Fluorophore-Labeled Substrate

Jiahui Wu,[†,▽] Dengyou Zhang,[‡,▽] Lei Chen,[†] Jianneng Li,[⊥] Jianling Wang,[§] Chengqing Ning,[#] Niefang Yu,[#] Fei Zhao,[‡] Dongying Chen,[§] Xiaoyan Chen,[∥] Kaixian Chen,[‡] Hualiang Jiang,[‡] Hong Liu,*[,‡] and Dongxiang Liu*[,†,¶]

[†]Department of Pharmacology III, [‡]Drug Discovery and Design Center, [§]Department of Analytical Chemistry, and [∥]Center for Drug Metabolism and Pharmacokinetics, Shanghai Institute of Materia Medica, Chinese Academy of Sciences, 555 Zu-Chong-Zhi Road, Shanghai 201203, China

[⊥]School of Life Sciences, Fudan University, Shanghai 200433, China

[#]Institute of Molecular Design and Drug Discovery, School of Pharmaceutical Sciences, Central South University, Changsha 410078, Hunan, China

Supporting Information

ABSTRACT: SIRT1 is an NAD^+-dependent deacetylase, whose activators have potential therapeutic applications in age-related diseases. Here we report a new class of SIRT1 activators. The activation is dependent on the fluorophore labeled to the substrate. To elucidate the activation mechanism, we solved the crystal structure of SIRT3/ac-RHKK$_{ac}$-AMC complex. The structure revealed that the fluorophore blocked the H-bond formation and created a cavity between the substrate and the Rossmann fold. We built the SIRT1/ac-RHKK$_{ac}$-AMC complex model based on the crystal structure. K_m and K_d determinations demonstrated that the fluorophore decreased the peptide binding affinity. The binding modes of SIRT1 activators indicated that a portion of the activators interacts with the fluorophore through π-stacking, while the other portion inserts into the cavity or interacts with the Rossmann fold, thus increasing the substrate affinity. Our study provides new insights into the mechanism of SIRT1 activation and may aid the design of novel SIRT1 activators.

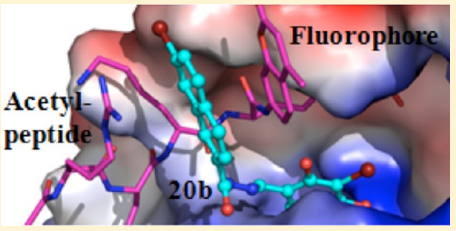

INTRODUCTION

Sirtuins are a class of protein deacetylases that belong to KDAC family. Unlike other KDACs, the deacetylation by sirtuins requires the involvement of nicotinamide adenine dinucleotide (NAD^+).[1] Mammal possesses seven sirtuins (SIRT1−SIRT7), and they are widely distributed in different subcellular compartments.[2] SIRT1, SIRT6, and SIRT7 are localized in the nucleus, while SIRT2 is in the cytoplasm and SIRT3, SIRT4, and SIRT5 are in mitochondria. Among them, SIRT1 shares the highest sequence homology with yeast sirtuin information regulator 2 (Sir2) and is the most extensively studied.

SIRT1 deacetylates a broad range of substrates and plays important roles in many biological functions. For instance, SIRT1 deacetylates histone H1 and promotes the heterochromatin formation.[3] H3 and H4 could be deacetylated by SIRT1 and the RNA interference of SIRT1 induced hyperacetylation of the two proteins in human cells.[4] SIRT1 binds to the fat regulator peroxisome proliferator activated receptor γ (PPARγ) and represses the genes controlled by PPARγ. Studies revealed that overexpression of SIRT1 attenuates the adipogenesis.[5] Also, adiponectin transcription could be enhanced by SIRT1 in adipocytes through activating FOXO1[6] and cell resistance to oxidative stress could be increased by SIRT1 through regulating FOXO family of Forkhead transcription factors.[7] Besides, SIRT1 can regulate the genes involved in insulin secretion in pancreatic β cell lines and β cell-specific SIRT1-overexpressing (BESTO) mice by repressing uncoupling protein 2 (Ucp2).[8,9] Additionally, SIRT1 promotes glucose homeostasis and mitochondrial biogenesis through PPARγ coactivator 1α (PGC-1α).[10,11] Therefore, SIRT1 is involved in a wide range of physiological activities including fatty acid oxidization, stress resistance, insulin secretion, and glucose production, which are closely related to age-related diseases such as type 2 diabetes, cardiovascular disease, metabolic syndrome, inflammation, and also to aging and longevity.[12,13] Development of SIRT1 activators has potential therapeutic applications in the treatment of the age-related diseases.

Up to the present, several SIRT1 activators were identified (Figure 1). They could be mainly categorized into two classes: natural plant polyphenols and synthesized small molecules. **1** (resveratrol) and several other plant polyphenols were first discovered by using a fluorescent assay with a fluorophore-labeled peptide as the substrate.[14] Treatment of *Saccharomyces cerevisiae* with **1** significantly increased the life span of the yeast. Studies in *Caenorhabditis elegans*,[15] *Drosophila*,[15,16] and

Received: July 13, 2012
Published: January 14, 2013

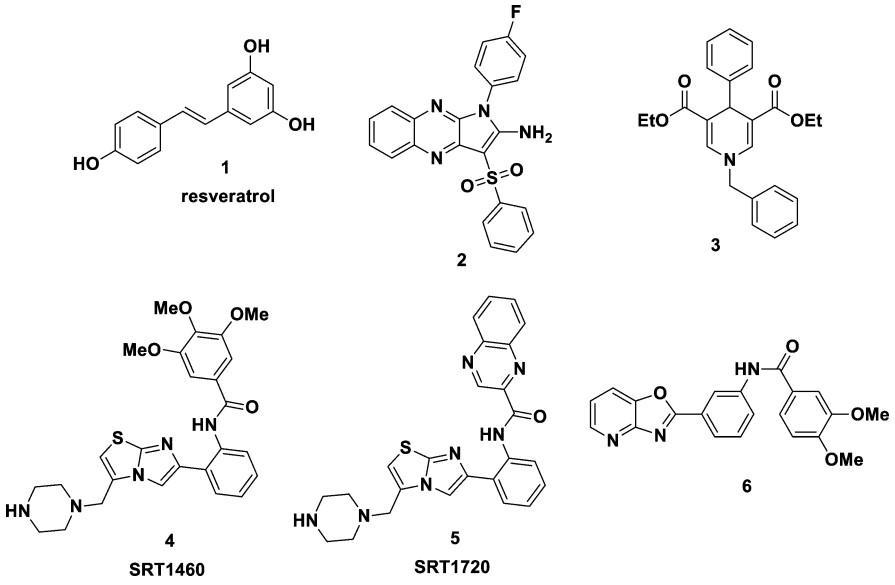

Figure 1. Chemical structures of representative SIRT1 activators.

vertebrates[17] had proven the positive effect of **1** in increasing the life span. Besides, **1** was found to attenuated insulin resistance under high-fat diet induced conditions in vivo,[18] and treatment of type 2 diabetic mice with **1** induced mitochondrial biogenesis.[19] Meanwhile, small molecules with structures unrelated to **1** had been identified to activate SIRT1 in vitro by using the fluorophore-labeled substrates, which include compound **2**,[20] **3**,[21] and the compounds discovered by the Sirtris company like **4** (SRT1460), **5** (SRT1720),[22,23] and **6**[24] (Figure 1).

However, it is still controversial whether **1** and Sirtris compounds are real SIRT1 activators. In vitro studies revealed that the activation of SIRT1 by these compounds requires the fluorophore attached to the peptide substrate, and the activation could not be observed in deacetylating the substrate lacking of fluorophore.[25,26] Even though Dai et al. provided the biophysical evidence of the direct binding between the Sirtris compounds and SIRT1, they suggested that the activators bind in an allosteric site of the enzyme.[27] In terms of in vivo effect of **1**, in contrast with the positive results mentioned above, some studies showed that there is neither detectable effect of **1** on Sir2 activity in yeast[25] nor significant effect on lifespan in *Drosophila*.[28] As for the SIRT1 small molecule activator **5**, some results indicated that it could ameliorate insulin sensitivity and glucose tolerance in obese mice[22,29] and enhance mitochondrial biogenesis in mice fed with a high calorie diet,[30] whereas Pacholec et al. reported that no effect of lowering plasma glucose or improving mitochondrial capacity could be detected in mice.[26]

Considering the numerous and paradoxical reports about SIRT1 activators, obviously it is very important to elucidate the activation mechanism of the activators on molecular level. In this study, a series of diaryl acylhydrazone compounds with the activation activities of SIRT1 were first identified from our in-house compound library by employing a coumarin-labeled acetyl peptide. We synthesized a series of analogues of these compounds and established their structure−activity relationship. Combining the protein crystallography, molecular modeling, and site-directed protein mutagenesis, we determined the binding site of our compounds, **1** and **4**. The activity, stability, and bioavailability of our compounds were also tested on cell level. Our goal is to explain the substrate selectivity and the activation mechanism of these SIRT1 activators from the structural point of view. The mechanism of SIRT1 activation by small molecules presented here may shed light in the design of SIRT1 novel activators.

RESULTS AND DISCUSSION

Identification of Chemical Compounds That Enhance SIRT1 Enzyme Activity. A high-throughput fluorescent assay was deployed to screen our in-house compound library aiming to discover novel SIRT1 activators. To our delight, five compounds based on diaryl acylhydrazone scaffold were identified with the activation effect of SIRT1 deacetylation (Table 1). Notably, our compounds displayed $EC_{1.5}$ values ranging from 1.6 to 7.0 μM and the highest maximum activation was up to 375%. The $EC_{1.5}$ values were better than that of **1** ($EC_{1.5}$ of **1** was 23.6 μM). These results encouraged us to further optimize the diaryl acylhydrazone scaffold. Our efforts were mainly focused on diversifying the aryl fragments due to their convenient modification.

Synthesis of Diaryl Acylhydrozone Analogues. Compounds **16a−n** were prepared according to Scheme 1. Suzuki coupling of methyl 4-bromobenzoate **12a** with aryl bromide or 4-(methoxycarbonyl)phenylboronic acid **12b** with aryl boric acid smoothly afforded biphenyl esters **13a−k**. Hydrazinolyzation of **13a−k** and **12c** gave hydrozide intermediate **14a−k**. Condensation of **14a−k** with benzaldehyde moieties **15a−d** readily provided compounds **16a−k**. **15b−d** were prepared according to the refs 31 and 32. Preparation of compounds **16l−n** was from commercial available hydrazides **17l−n**. Naphthyl analogues **20a−i** were synthesized in a similar manner as **16a−n** (Scheme 2). The details of the synthetic procedures and structural characterizations are described in the Experimental Section.

Structure−Activity Relationship (SAR) of Diaryl Acylhydrazone Analogues. The activation curves of representative compounds were shown in Figure 2. Initial observation of the activities (Table 1) revealed that the compound bearing the *p*-Cl phenyl group (**9**) seemed to be inferior to analogues with the biphenyl (**7**, **8**) or naphthyl

dx.doi.org/10.1021/jm301032j | J. Med. Chem. 2013, 56, 761−780

Table 1. The Activities of the Initial Hits Identified by Our Fluorescent Assay[c]

Compound	Structure	$EC_{1.5}$ (μM) [a]	Max A (%) [b]
1	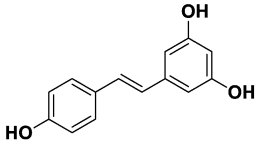	23.6	802
7	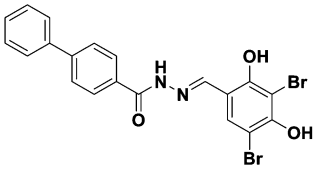	1.7	246
8	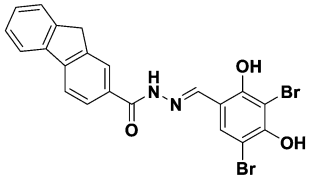	5.4	212
9	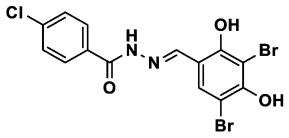	7.0	174
10	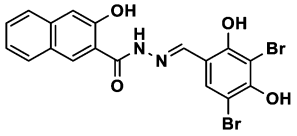	4.5	375
11	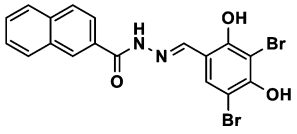	1.6	331

[a]$EC_{1.5}$ value represents the concentration of an activator required to increase the enzyme activity by 50%. [b]Percentage of maximum activation achieved. [c]For comparison, the activity of compound **1** was also listed in this table.

Scheme 1. Synthesis of Compounds 16a−n[a]

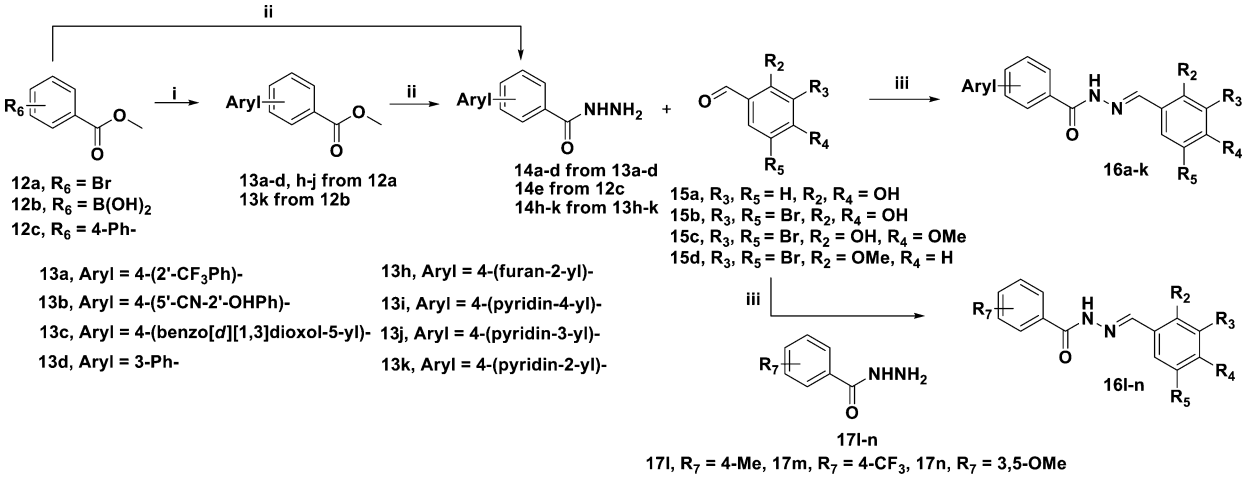

[a]Reagents and conditions: (i) $Pd(PPh_3)_4$, $KF{\cdot}2H_2O$, DME/H_2O/EtOH (7:3:2), M_w, 110 °C; (ii) $N_2H_4{\cdot}H_2O$, MeOH, reflux; (iii) AcOH, EtOH, reflux.

dx.doi.org/10.1021/jm301032j | J. Med. Chem. 2013, 56, 761−780

Scheme 2. Synthesis of Compounds 20a–i[a]

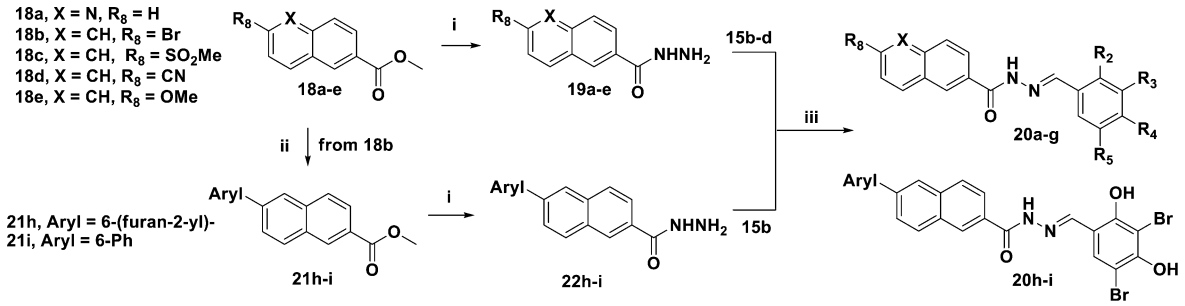

[a]Reagents and conditions: (i) $Pd(PPh_3)_4$, $KF{\cdot}2H_2O$, DME/H_2O/EtOH (7:3:2), M_w, 110 °C; (ii) $N_2H_4{\cdot}H_2O$, MeOH, reflux; (iii) AcOH, EtOH, reflux.

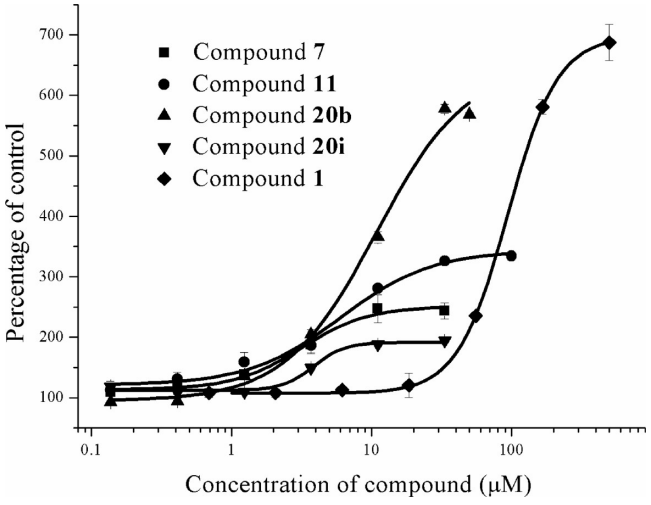

Figure 2. The dose–response curves of our compounds and **1** measured by the fluorescent assay.

groups (**10**, **11**). Changing the *p*-Cl phenyl group to other phenyl groups such as *p*-tolyl (**16l**) and *p*-CF_3 phenyl (**16m**) groups slightly reduced the activity (Table 2). Introduction of 3,5-dimethoxyl phenyl (**16n**) group notably weakened SIRT1 activation. These results suggested that the modification of phenyl group might not give rise to remarkable gain of the activity, which turned our attention to optimize biphenyl and naphthyl analogues.

Compared with the parent compound **7** ($EC_{1.5}$ = 1.7 μM, maximum activation = 246%), introduction of various substituted phenyl moieties **16a–c** at the C-4 position (P2 Part) retained the comparable activity whereas the C-3 substituted analogue **16d** exhibited 10-fold less activity ($EC_{1.5}$ = 18.3 μM), indicating that a linear fragment was preferred over a branched fragment. 3,5-Dibromide substituents (P1 part) were shown to play an important role in binding affinity because the removal of two bromide **16e** resulted in a drop-off of $EC_{1.5}$ (10.4 μM). Methylation of either hydroxy group (**16f** and **16g**) also eroded the activity, which indicated that both hydroxyl groups at C-2 and C-4 positions (P1 part) might function as hydrogen donors. Replacement of the phenyl moieties with heteroaryl groups (P2 part) such as furan **16h** and pyridine **16i–k** maintained the similar $EC_{1.5}$ but with the improvement of the maximum activation.

Next, a series of naphthyl analogues were explored (Table 3). Interestingly, replacement of the naphthalene **11** ($EC_{1.5}$ = 1.6 μM, maximum activation = 331%) with the quinoline **20a** ($EC_{1.5}$ = 55.2 μM) resulted in a sharp decrease of the activity. Introduction of the bromide (**20b**) at the C-6 position of the naphthalene (P2 part) displayed a similar $EC_{1.5}$ (2.7 μM) but with the improvement of maximum activation up to 647%. A block of either hydroxyl at the C-2 and C-4 positions (P1 part) using methyl group (**20c** and **20d**) was not beneficial for the potency, which was also observed in biphenyl analogues. Changing the bromide to electron-withdrawing groups such as a methylsulfonyl (**20e**) or a cyano group (**20f**) gave rise to a decrease of maximum activation. Appending the methoxy group (**20g**) increased the $EC_{1.5}$ to 0.9 μM and the maximum activation to 624%, which showed the highest activation potency among the compounds. Although the incorporation of furan (**20h**) and benzene (**20i**) at the C-6 position of the naphthalene (P2 part) maintained a comparable $EC_{1.5}$, the maximum activation tended to decrease.

To examine the selectivity of the SIRT1 activators, we tested their activities on SIRT1 and its closest sirtuin homologues: SIRT2 and SIRT3. The compounds were tested at the concentration of 50 μM. The data for SIRT1, SIRT2, and SIRT3 were listed in Supporting Information Table S1. The $EC_{1.5}$ values for SIRT2 and SIRT3 of the compounds unmentioned in the following parentheses were greater than 50 μM (SIRT2: **8**, $EC_{1.5}$ = 16.5 μM, maximum activation = 206%. **20i**, $EC_{1.5}$ = 11.6 μM, maximum activation = 257%. SIRT3: **20i**, $EC_{1.5}$ = 28.6 μM, maximum activation = 199%.). The results showed that these compounds (**1**, **7–11**, **16a–n**, **20a–i**) are selective for the activation of SIRT1.

Compounds Promote the Deacetylation of Fluorophore-Labeled Peptide but Not the Unlabeled Peptide. Further, we tested the activities of **20b**, **1**, and **4** on fluorophore-unlabeled acetyl peptide. A known SIRT1 inhibitor, 6-chloro-2,3,4,9-tetrahydro-1*H*-carbazole-1-carboxamide (Ex527), was used as control.[33] Acetyl-Arg-His-Lys-Lys (ε-acetyl)-NH_2 peptide (ac-RHKK$_{ac}$-NH_2) was synthesized without 4-amino-7-methylcoumarin (AMC) labeled at the C-terminus. The deacetylation reactions of the unlabeled peptide were carried out in the same way as the AMC-labeled peptide. The amount of deacetylated peptide was determined by HPLC. Deacetylation enhancement by compound **20b** was observed with the AMC-labeled peptide but not the unlabeled peptide (Supporting Information Figure S3 and Figure 3). Inconsistent with previous reports,[25,26] **1** and **4** did not activate SIRT1 in deacetylating the fluorophore-unlabeled peptide. This phenomenon aroused our guess that the compounds do not bind directly with SIRT1 but bind to the "SIRT1/fluorophore-labeled peptide" complex. ITC experiments carried out by Milne et al. and Pacholec et al. also support the conjecture.[22,26]

dx.doi.org/10.1021/jm301032j | J. Med. Chem. 2013, 56, 761–780

Table 2. Structures and Activities of the Biphenyl and Phenyl Hydrazones[d]

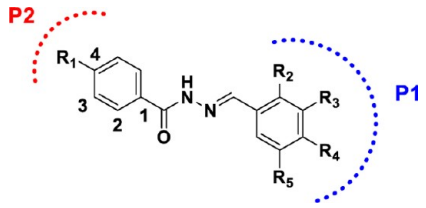

Compound	R_1	R_2	R_3	R_4	R_5	$EC_{1.5}$ (μM) [a]	Max A (%) [b]
16a	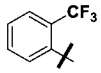	OH	Br	OH	Br	0.9	216
16b	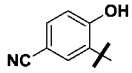	OH	Br	OH	Br	3.7	196
16c	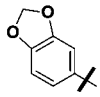	OH	Br	OH	Br	3.4	380
16d*	3-Ph	OH	Br	OH	Br	18.3	212
16e		OH	H	OH	H	10.4	157
16f		OH	Br	OMe	Br	28.1	242
16g		OMe	Br	OH	Br	18.1	191
16h		OH	Br	OH	Br	2.1	374
16i		OH	Br	OH	Br	1.6	390
16j		OH	Br	OH	Br	2.0	314
16k		OH	Br	OH	Br	2.3	467
16l	Me	OH	Br	OH	Br	9.6	161
16m	CF_3	OH	Br	OH	Br	20.5	161
16n#	3,5-dimethoxy	OH	Br	OH	Br	ND [c]	112

[a] $EC_{1.5}$ value represents the concentration of an activator required to increase the enzyme activity by 50%. [b] Percentage of maximum activation achieved. [c] None detected. [d] * = R_1 at C-3 position; # = R_1 at C-3 and C-5 position.

When **4** was titrated to SIRT1-substrate (Tamra-labeled peptide) mixture, the binding was observed.[22,26] However, no binding isotherm was observed when **4** was titrated to SIRT1 and fluorophore-unlabeled peptide solution.[26] Thus, we believe that the fluorophore linked to the peptide is the key element for the binding activity.

Crystal Structure of ac-RHKK$_{ac}$-AMC Peptide in Complex with SIRT3. To confirm the role of the fluorophore, we tried to determine the conformation of the fluorophore conjugated with the peptide inside the enzyme. Up to now, the structures of several sirtuin proteins were solved, including Hst2 and Sir2p of yeast, Sir2-Af1 and Sir2-Af2 of archaea, Sir2Tm of bacteria, and SIRT2, SIRT3, SIRT6, and SIRT7 of humans. However, the structure of SIRT1 is still uncovered due to the aggregation feature of the protein. Both sequence alignment and structure superposition of the sirtuin homologues revealed that they share high sequence homology as well as structure homology.[34] This suggests that SIRT1 model may

dx.doi.org/10.1021/jm301032j | J. Med. Chem. 2013, 56, 761−780

Table 3. Structures and Activities of the Naphthohydrazones

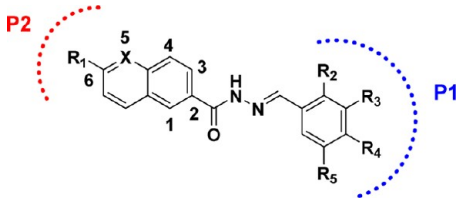

Compound	R_1	X	R_2	R_3	R_4	R_5	$EC_{1.5}$ (μM) [a]	Max A (%) [b]
20a	--	N	OH	Br	OH	Br	55.2	239
20b	Br	C	OH	Br	OH	Br	2.7	647
20c	Br	C	OH	Br	OMe	Br	ND [c]	119
20d	Br	C	OMe	Br	OH	Br	8.7	298
20e	$MeSO_2$	C	OH	Br	OH	Br	2.3	368
20f	CN	C	OH	Br	OH	Br	4.4	433
20g	OMe	C	OH	Br	OH	Br	0.9	624
20h		C	OH	Br	OH	Br	2.6	267
20i		C	OH	Br	OH	Br	1.8	194

[a] $EC_{1.5}$ value represents the concentration of an activator required to increase the enzyme activity by 50%. [b] Percentage of maximum activation achieved. [c] None detected.

Table 4. Data Collection and Refinement Statistics of "SIRT3/ac-RHKK$_{ac}$-AMC" Complex

diffraction data	
space group	*R*32
resolution (Å)[a]	50−2.1 (2.18−2.10)
unit cell parameters	
a, *b*, *c* (Å)	114.809, 114.809, 123.202
α, β, γ (deg)	90.00, 90.00, 120.00
completeness (%)[a]	99.9 (100.0)
redundancy[a]	11.0 (11.1)
average $I/\sigma I$[a]	24.8 (4.4)
R_{merge} (%)[a]	10.0 (66.5)
refinement statistics	
$R_{working}$ (%)	20.76
R_{free} (%)	28.19
rmsd in bond length (Å)	0.0242
rmsd in bond angles (deg)	2.0687
mean *B*-factors	45.762
Ramachandran plot	
in preferred regions (%)	93.85
in allowed regions (%)	6.15
outliers (%)	0.00

[a] Values for the highest resolution shells are represented in parentheses.

be built based on its homologue protein. According to the sequence alignment of SIRT1 and SIRT3 (Supporting Information Figure S4), the two proteins showed very high sequence homology in the catalytic region. The differences between SIRT1 and SIRT3 sequences were at the flexible loop connecting the zinc-binding motif and Rossmann fold region (between α2 and α3), a turn in the zinc-binding motif (between α9 and β6), and a short α-helix on the Rossmann fold domain (α12). These amino acids are distributed mainly on the surface of SIRT3 protein, which are far away from the acetyl peptide binding site. Because our attention was focused on the

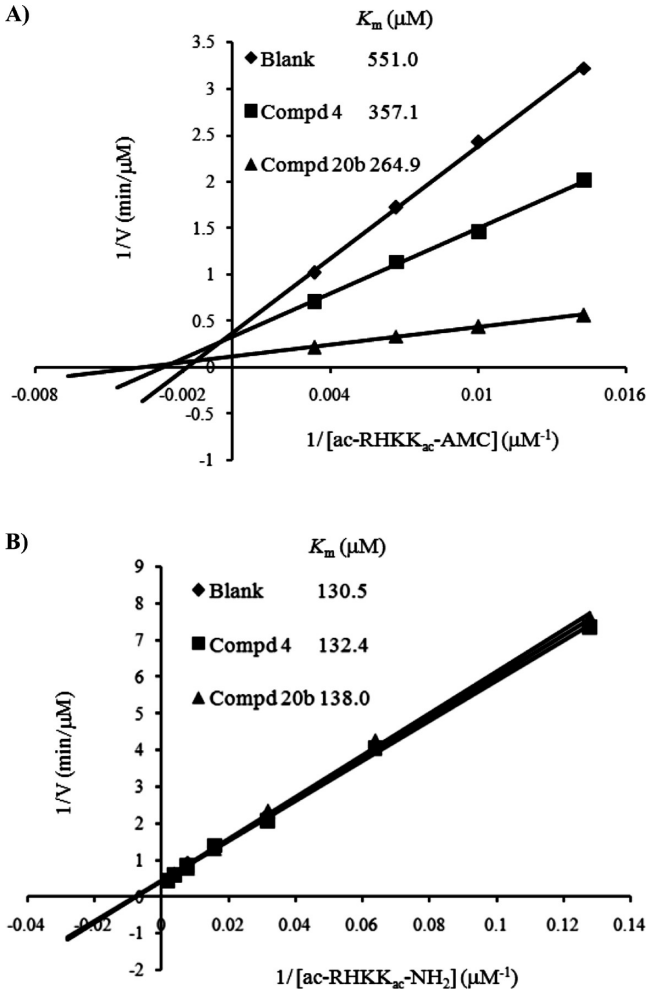

Figure 3. The Lineweaver−Burk plots of (A) ac-RHKK$_{ac}$-AMC peptide and (B) ac-RHKK$_{ac}$-NH$_2$ peptide in the presence of 50 μM **4** and 10 μM **20b**, which were determined by HPLC method. **4** and **20b** exhibited substrate selectivity against native peptide and fluorophore-labeled peptide.

peptide binding site, the catalytic core domain of SIRT1 could be built by using the structure of SIRT3 as template. Thus, SIRT3 was chosen for cocrystallization with the AMC-labeled acetyl peptide.

The purified SIRT3 protein was incubated with ac-RHKK$_{ac}$-AMC peptide at 4 °C overnight. The mixture was screened with Hampton Research kits by using the hanging-drop method at 15 °C. After two weeks, crystals were obtained with crystallization solution containing 0.085 M Hepes-Na (pH 7.5), 8.5% (v/v) isopropyl alcohol, 17% (w/v) polyethylene glycol (PEG) 4000, and 15% (v/v) glycerol anhydrous. The X-ray diffractions of the crystals were collected at Shanghai Synchrotron Radiation Facility. The data was processed by HKL2000[35] and ccp4 suite.[36] The data collection and refinement statistics of the complex structure were listed in Table 4. The space group of the complex is *R*32, which has one molecule in an asymmetric unit. Interestingly, the AMC-labeled peptides are involved in a "head-to-head" packing, which makes the complexes exhibiting a dimeric arrangement (Figure 4A,B). The acetyl-lysine (ALY) of the substrate inserts into the cleft between the zinc-binding motif (small domain) and the Rossmann fold region (large domain). The coumarins of the two peptide substrates are in sandwich stacking, with the side

dx.doi.org/10.1021/jm301032j | J. Med. Chem. 2013, 56, 761−780

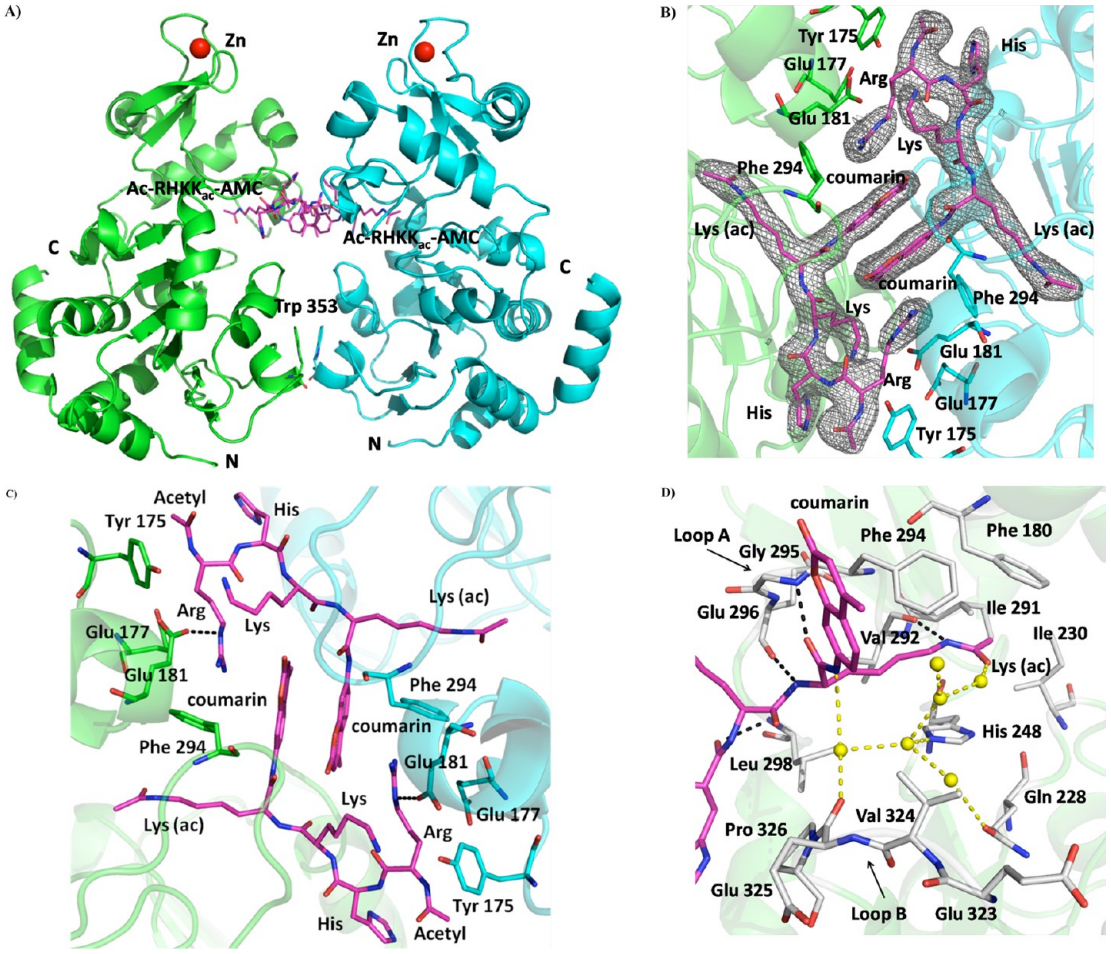

Figure 4. Structure of human SIRT3 in complex with substrate ac-RHKK$_{ac}$-AMC. (A) Ribbon diagram of the overall structure of the complexes in dimer. One molecule of SIRT3 protein is shown in green and the other in cyan. The substrate is shown in a stick representation; carbon, oxygen, and nitrogen are colored in magentas, red, and blue, respectively. Zinc ions are highlighted in red. (B) An enlarged view of the binding site in dimeric arrangement. The coumarin fluorophores of the substrates are packed in a "head-in-head" conformation, and the two peptides are represented with the $2F_o - F_c$ electron density maps (1.0 σ-contoured). The labeled amino acids are involved in the packing. (C) The detailed interaction of Figure 4B without map. The black dashed lines represent the H-bonds formed between the substrate and the residues. (D) An enlarged view of the active site in an asymmetric cell. Four hydrogen bonds (represented with black dashed lines) are formed between the substrate and the protein. Water molecules are represented with yellow spheres, and the H-bond interactions of waters are shown as yellow dashed lines. Loop A and loop B were indicated with arrows.

chain of arginine from another substrate packing aside the fluorophore. Because of such substrate arrangement, the two protein molecules are packed in a little twisted "shoulder-in-shoulder" conformation. Moreover, the π-stacking was also observed in the side chains of Trp 353 of two protein molecules (Figure 4A). Though the dimerization of the fluorophores was observed under the crystallization condition, the complex structure suggests that the coumarin may intact with other aromatic rings such as small molecules under physiological conditions in like manner. This is because the configuration of a single aromatic fluorophore is energetically unfavorable at physiological conditions due to its high hydrophobicity and lacking of significant contacts with the protein. The interaction with another aromatic ring may stabilize the configuration of the fluorophore.

The interaction details around the coumarins of two complex molecules were shown in Figure 4C. As described above, the arginine of one substrate packs head-to-head with the coumarin from another substrate. The γ-guanido group of arginine is usually protonated at physiological conditions. It may form cation$-\pi$ interaction with the coumarin and Phe 294. Also, the arginine forms an H-bond with the carboxyl of Glu 181 of another protein molecule. The alkyl side chain of the arginine and the N-terminal acetyl group of the peptide are in van der Waals interactions with Tyr 175 and Glu 177 from another protein molecule. Besides, the phenyl group of Phe 294 hangs over the AMC fluorophore in a T-shaped stacking and the packed fluorophores are sandwiched by the arginine and Phe 294 at each side.

As shown in the enlarged view of the binding site in monomer (Figure 4D), the substrate is trapped by a loop (SIRT3−291−299) with its ALY protruding into the active site. The loop between β6 and α10 on the small domain was defined as loop A (Supporting Information Figure S4). The residues on loop A formed four H-bonds with the peptide (Val 292, Gly 295, Glu 296, and Leu 298). These H-bonds are strong drive forces that entrap the substrate to the protein cavity. His 248 is conserved in mammal sirtuins and critical for the deacetylase activity.[37−39] The acetyl group of the substrate lysine is in between Phe 180 and His 248. Meanwhile, residues of Ile 291 and Ile 230 (both are conserved in mammal sirtuins) surround the methyl group of the ALY through van der Waals

dx.doi.org/10.1021/jm301032j | J. Med. Chem. 2013, 56, 761−780

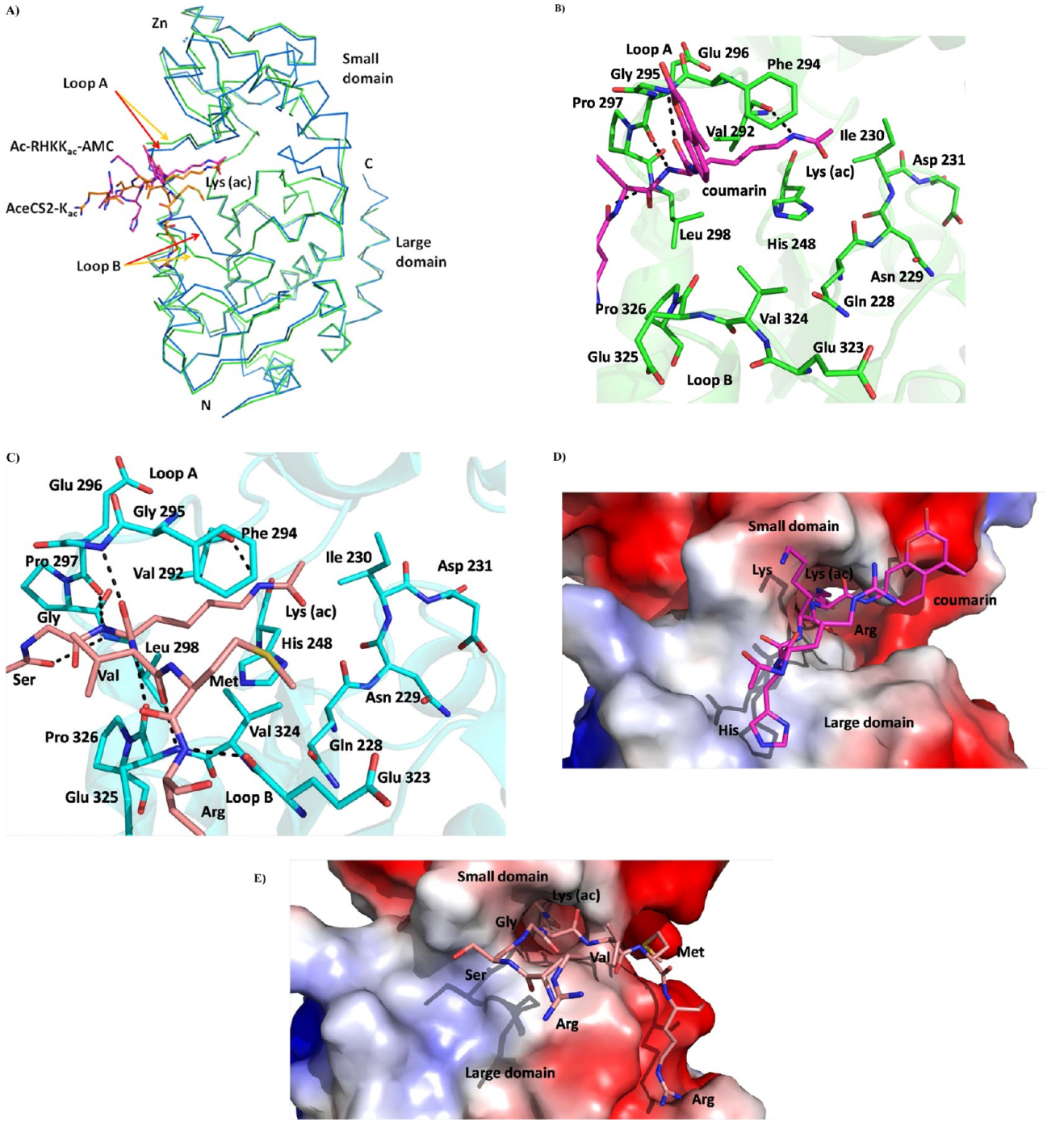

Figure 5. Structure comparison of SIRT3 protein in complex with AceCS2-K$_{ac}$ peptide (RSGK$_{ac}$VMR) and ac-RHKK$_{ac}$-AMC peptide. (A) The structure alignment of SIRT3 in complex with two peptides. The "SIRT3/ac-RHKK$_{ac}$-AMC" structure is colored in green with the peptide in stick representation and carbon atoms colored in purple. The "SIRT3/AceCS2-K$_{ac}$" structure is colored in slate with the carbon atoms of the peptide colored in orange. In the loop region (SIRT3−159−167), no density map was observed in the "SIRT3/ac-RHKK$_{ac}$-AMC" structure. Loop A and loop B on the ALY binding site were indicated with arrows (red arrows for "SIRT3/AceCS2-K$_{ac}$" and orange arrows for "SIRT3/ac-RHKK$_{ac}$-AMC"). (B) An enlarged view of the binding site in the structure of "SIRT3/ac-RHKK$_{ac}$-AMC". The peptide forms four H-bonds with the residues on the small domain. (C) An enlarged view of the binding site in the structure of "SIRT3/AceCS2-K$_{ac}$". The peptide forms four H-bonds with the residues on loop A and three H-bonds with that on loop B. The distances between the acetyl-lysine and loop B of the "SIRT3/AceCS2-K$_{ac}$" structure were shorter than that of the "SIRT3/ac-RHKK$_{ac}$-AMC" structure. (D) A lateral view of the binding site in (B). The protein molecule is in electrostatic surface representation. (E) A lateral view of (D).

interactions. In the structure, the binding cavity is filled with water molecules as shown in Figure 4D. The water not only formed H-bond interactions between each other but also interacted with residues Gln 228, His 248, and Glu 325 of SIRT3, the acetyl group of ALY, and the linker of coumarin.

Structure Comparison of SIRT3 in Complex with Different Acetyl Peptides. Jin et. al reported the structure of SIRT3 in complex with its substrate AcsCS2-K$_{ac}$ (PDB ID: 3GLR).[40] The sequence of the peptide is TRSGK$_{ac}$VMRRLLR. Only the region of RSGK$_{ac}$VMR was observed in the crystal

dx.doi.org/10.1021/jm301032j | J. Med. Chem. 2013, 56, 761−780

structure. As for other sirtuin−peptide complex, the ALY of the substrate inserts into the cleft between the small and large domains. loop A as well as a loop on the large domain (SIRT3−323−326 in between β7 and α11, defined as loop B) and the peptides form an enzyme−substrate antiparallel β-sheet. The AcsCS2-K_{ac} peptide pulls two loops closer to each other in comparison with those in the apo-SIRT3 structure (PDB ID: 3GLS). This suggests that binding of the acetyl peptide induced a conformational change of the enzyme.

To examine whether the binding of the fluorophore-labeled peptide may induce further conformational change of the cleft, we superimposed the "SIRT3/AMC-acetyl peptide" complex structure with the "SIRT3/AcsCS2-K_{ac} peptide" complex structure. The overall structures of SIRT3 in complex with two peptides are similar. The root-mean-square deviation (rmsd) of the C_α atoms of SIRT3 in the two complexes was 0.97 Å. As shown in Figure 5A, the main difference was at the cleft in between loop A and loop B. In the "SIRT3/ac-RHKK$_{ac}$-AMC" structure, the distance between the two loops increased and the cleft adopted a more open conformation. We speculated that the wider formation of the cleft was due to the steric block of the coumarin. As shown in Figure 5B, the residues on loop B from the large domain did not form any direct interaction with the peptide. Only the carbonyl oxygen of Glu 325 had indirect connection with the peptide via the H-bond network of the water molecules (Figure 4D). The vertical orientation of the coumarin seems to repel the hydrogen bonding between the substrate and the large domain, while for AcsCS2-K_{ac} peptide in the SIRT3 complex, the residues after ALY formed three H-bonds with the residues on loop B (Figure 5C). The comparison of the protein surface at the binding sites clearly showed that the clefts in the complexes adopted different conformations due to the features of the acetyl substrates (Figure 5D,E).

Complex Model of SIRT1 with ac-RHKK$_{ac}$-AMC Peptide. To elucidate the activation mechanism of our compounds, we built a SIRT1 model using SIRT3 as the template by homology modeling. The sequence of SIRT1 (244−498) was aligned with SIRT3 (Supporting Information Figure S4). In the "SIRT3/ac-RHKK$_{ac}$-AMC" complex, no density map was observed in the region of SIRT3−158−167, which is a flexible loop on the protein surface. Thus, the structure at the regions of 121−157 and 168−391 of "SIRT3/ac-RHKK$_{ac}$-AMC" complex and the loop region (158−167) of SIRT3-AcsCS2-K_{ac} complex (PDB ID: 3GLR) were used as the templates. After structural refinement, the coordinates of AMC-labeled peptide were copied from "SIRT3/ac-RHKK$_{ac}$-AMC" complex to the SIRT1 model. The "SIRT1/ac-RHKK$_{ac}$-AMC" complex model was submitted to further structural refinement.

The complex model of SIRT1 was shown in Figure 6A. The cleft adopted an open conformation as the "SIRT3/ac-RHKK$_{ac}$-AMC" structure did. As shown in Figure 6B, the peptide is captured by the loop of SIRT1−411−419 which corresponds to loop A. Hydrogen bond interactions were formed between the peptide and the backbone atoms of SIRT1 residues on loop A (Val 412, Gly 415, Glu 416, and Leu 418). The phenyl ring of Phe 414 is adjacent to the AMC fluorophore. The acetyl group of the lysine is sandwiched by the phenyl ring of Phe 297 and imidazole ring of His 363. The side chains of Ile 347 and Ile 411 form van der Waals interactions with the methyl group of the ALY. All the residues mentioned above are conserved in SIRT1 and SIRT3. The binding mode is similar with the

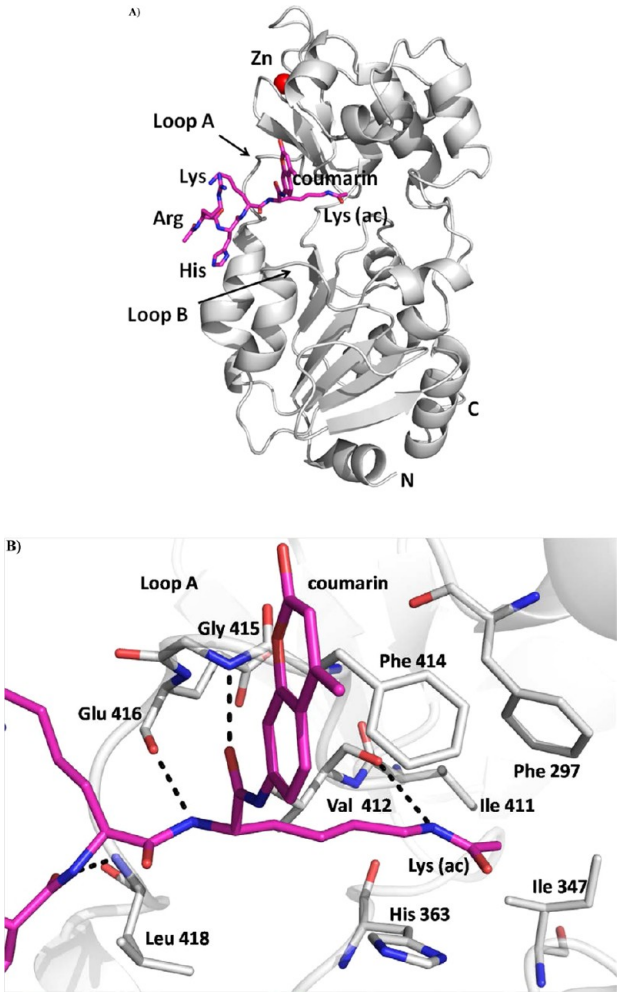

Figure 6. The homology model of SIRT1 in complex with ac-RHKK$_{ac}$-AMC peptide. (A) The overall structure of the complex model. SIRT1 is represented in cartoon and colored in silver. Loop A and loop B were indicated with arrows. (B) The binding site of the complex. The peptide forms four H-bonds with the backbone atoms on loop A.

SIRT3−substrate complex. The substrate did not have direct interaction with the residues from loop B.

According to the sirtuin catalytic mechanism, the carbonyl oxygen at the side chain of ALY carries out nucleophilic attacks to the C1′ position of the *N*-ribose of NAD^+, which initiates the deacetylation. After that, an *O*-alkylamidate intermediate was formed.[41] We suppose that the broadening of the cleft and the relative position shift of residues involved in catalysis may hinder the hydrolysis step in deacetylation. The fluorophore, whether it is coumarin or TAMRA, certainly will cause steric block in the cleft due to its big and rigid body. The increase of the distance between the two loops and the loss of the H-bonds between the substrate and the large domain will weaken the substrate binding. Both the kinetic experiment and ITC titration demonstrated that the existence of coumarin increased the K_m and K_d values of the peptide to SIRT1. The K_m values of two acetyl substrates (with or without coumarin) were 551.0 and 130.5 μM, respectively (Figure 3), and the K_d values calculated by titrating the peptide into SIRT1 were 184 and 44 μM, respectively (Supporting Information Figure S1). On the basis of above analysis, we built the binding modes of the activators and proposed their activation mechanism.

dx.doi.org/10.1021/jm301032j | J. Med. Chem. 2013, 56, 761−780

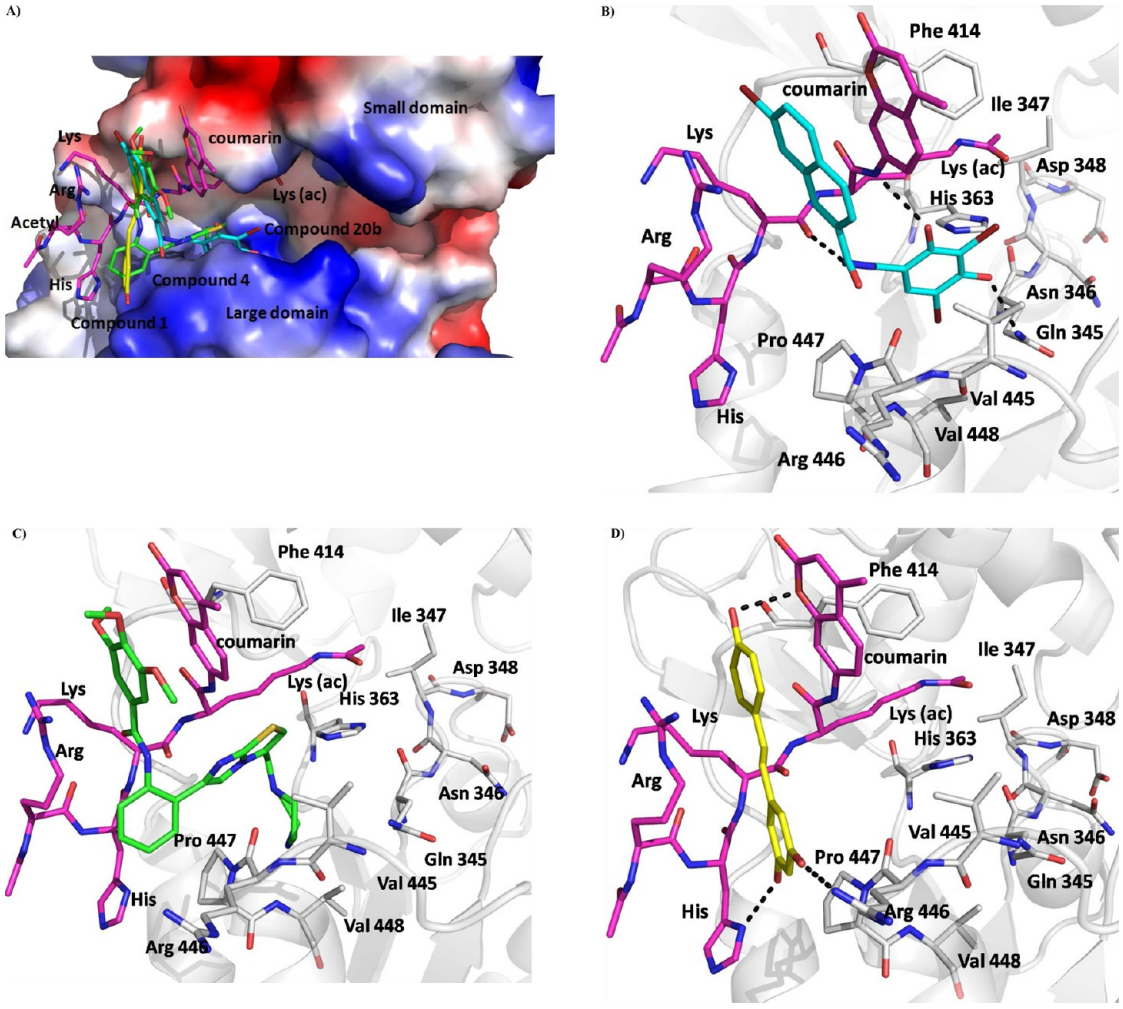

Figure 7. The binding modes of SIRT1 activators with "SIRT1/ac-RHKK$_{ac}$-AMC". (A) A superimposed view of three small compounds that bind to the complex. The fluorophore-labeled peptide is colored in magentas; compounds **20b**, **1**, and **4** are colored in cyan, yellow, and green, respectively. (B) An enlarged view of **20b** binding mode. The nitrogen atom on the linker forms hydrogen bond with the peptide. The *p*-hydroxyl on the 3,5-dibromo-2,4-dihydroxyphenyl fragment H-bonds with the amino group on the side chain of Gln 345, while the *o*-hydroxyl H-bonds with the linker between the substrate and the coumarin. (C) An enlarged view of **4** binding mode. (D) An enlarged view of **1** binding mode. The two hydroxyls H-bond with the sides chains of Arg 446 and His of the substrate, respectively.

SIRT1 Activators Bind in the Broadened Cleft Caused by the Fluorophore. To explore the binding sites of the activators, compounds **20b**, **1**, and **4** were docked into "SIRT1/ac-RHKK$_{ac}$-AMC" complex model. The poses of **20b**, **1**, and **4** were superimposed in the complex model as shown in Figure 7A. Three compounds bound in the hydrophobic pocket formed by the side chains of His, Arg, Lys, and coumarin of the peptide and the residues at the large domain of SIRT1. All the compounds apparently have $\pi-\pi$ interactions with the coumarin.

Binding Mode of Diaryl Acylhydrazone Derivatives. In the "SIRT3/ac-RHKK$_{ac}$-AMC" crystal structure, two coumarins form π-stacking; therefore, we speculated that the activators may stack with the coumarin in the similar manner. As shown in Figure 7B, the 6-bromonaphthalene fragment of **20b** interacts with the coumarin in a "head-to-head" conformation, while the dibromo-dihydroxybenzaldehyde ring inserts into the cleft under the fluorophore. We monitored the hydrogen bonds between **20b** and "SIRT1/ac-RHKK$_{ac}$-AMC" complex; the *p*-hydroxyl on the dibromo-dihydroxybenzaldehyde ring interacts with the amino group from the side chain of Gln 345. According to the SAR, the hydroxyl is crucial in the activation, and methylation of the group resulted in a complete loss of the activity (compare **20b** and **20c**). Thus, the H-bond interaction is vital for the activation activity of our compounds. In the mechanism of sirtuin deacetylation, Gln 345 plays an important role. The carbonyl group on the side chain of Gln 345 may make an H-bond with 3′-OH of the ribose from NAD$^+$.[42,43] We speculated that the interaction between the compound and Gln 345 as well as other van der Waals interactions may stabilize the catalytic core and compensate the shifting induced by the coumarin; as a result, the V_{max} was accelerated. For the explanation of the K_m decrease (Figure 3A), we preferred that the activators caused tighter binding between the fluorophore-labeled peptide and SIRT1. In the previous publications, **1** and **4** were also proved to decrease the K_m values of the fluorophore-labeled peptides.[14,22,25,26] As shown in Figure 7B, besides the aromatic stacking, the imino group of **20b** makes an H-bond with the substrate, the *o*-hydroxyl on the dibromo-dihydroxybenzaldehyde fragment also H-bonds with the substrate. Through above interactions, compound **20b** increased the binding affinity of the substrate to the enzyme;

dx.doi.org/10.1021/jm301032j | J. Med. Chem. 2013, 56, 761−780

Table 5. The Kinetic Parameters of the ac-RHKK$_{ac}$-AMC Peptide to SIRT1 Wild-Type and Mutant Proteins[a]

(A)

		compound **20b**			blank	
	$EC_{1.5}$ (μM)[b]	Max A (%)[c]	K_m (μM)[d]	V_{max}/K_m[e]	K_m (μM)	V_{max}/K_m
SIRT1	2.7 ± 0.3	647	104.8 ± 8.8	13.1	240.4 ± 14.5	3.1
SIRT1^{Q345A}	12.2 ± 0.6	237	184.0 ± 3.7	1.0	262.6 ± 5.1	0.6
SIRT1^{V445A}	4.8 ± 0.2	353	191.0 ± 12.6	3.3	268.7 ± 22.9	1.8

(B)

		compound **1**			blank	
	$EC_{1.5}$ (μM)[b]	Max A (%)[c]	K_m (μM)[d]	V_{max}/K_m[e]	K_m (μM)	V_{max}/K_m
SIRT1	23.6 ± 3.4	802	111.3 ± 26.7	11.4	240.4 ± 14.5	3.1
SIRT1^{R446A}	87.2 ± 9.1	239	134.3 ± 14.6	4.4	256.2 ± 10.6	2.6

[a](A) The experiments were carried out in the absence or presence of 10 μM compound **20b**, respectively. (B) The experiments were carried out in the absence or presence of 50 μM compound **1**, respectively. [b]$EC_{1.5}$ value represents the concentration of an activator required to increase the enzyme activity by 50%. [c]Percentage of maximum activation achieved. [d]K_m, the concentration of substrate that results in half-V_{max} for an enzymatic reaction. [e]V_{max}, the maximum initial velocity of an enzymatic reaction.

Table 6. Structures and Activities of the Imidazo[1,2-*b*]thiazole Derivatives Identified by the Sirtris Group[a]

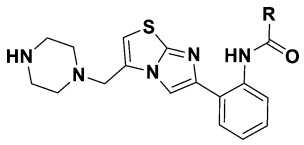

Compound	R	$EC_{1.5}$ (μM)[b]	Max A (%)[c]	Compound	R	$EC_{1.5}$ (μM)[b]	Max A (%)[c]
23		130	383	**28**		1.7	270
24		14	130	**29**	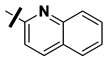	0.99	440
4	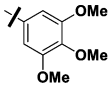	1.8	271	**5**	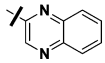	0.16	781
25	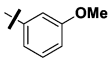	3.7	928	**30**	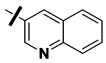	0.68	301
26	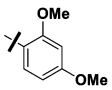	31	197	**31**		45	208
27		25	322	**32**	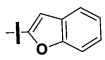	0.61	381
				33	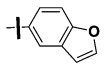	6.9	380

[a]The structures and SIRT1 activity data of the compounds came from table 2 in the ref 23. [b]$EC_{1.5}$ value represents the concentration of an activator required to increase the enzyme activity by 50%; [c]Percentage of maximum activation achieved.

the existence of **20b** in the broadened cleft may stabilize the complex conformation and facilitate the following catalysis.

We synthesized compounds with varying aromatic fragments at the P2 part (Tables 1, 2, and 3). The *m*-biphenyl substitution (**16d**) was less active than *p*-biphenyl (**7**). The orientation of the *m*-biphenyl is not favorable in the π-stacking with the coumarin. Introduction of electron-withdrawing group such as trifluoromethyl group (**16a**) and heterocyclic atoms oxygen (**16c**, **16h**) or nitrogen (**16i**, **16j**, and **16k**) to the biphenyl fragment maintained the activity as compared with **7**. The diaryl acylhydrazone derivatives with phenyl substitutions at P2 part exhibited weaker activities (**9**, **16l**, **16m**, and **16n**). In contrast, naphthalene substitutions significantly improved the activity. The substitution at the R_1 position of the naphthalene showed great tolerance (**20b**, **20e**, **20f**, **20g**, **20h**, and **20i**). The above SAR at the R_1 position is in line with our binding mode. Naphthalene substitution is preferred, and the substitutions on the naphthalene ring may improve the π-stacking.

To verify the binding mode, residues Gln 345 and Val 445, which were shown to have close contacts with **20b**, were

dx.doi.org/10.1021/jm301032j | J. Med. Chem. 2013, 56, 761−780

mutated for enzymatic activity and kinetic studies. In the binding mode, Gln 345 exhibited direct interaction with **20b** through the H-bond; in contrast, Val 445 showed much weaker interaction (van der Waals interaction) with **20b** (Figure 7B). Therefore, Gln 345 was mutated to alanine to eliminate the H-bond and Val 445 was mutated to alanine to alter the van der Waals interaction. The activation effects of compound **20b** to mutant proteins were shown in Supporting Information Figure S5 and listed in Table 5A. For SIRT1^{Q345A}, **20b** is about 4-fold less active to SIRT1^{Q345A} than to wild-type SIRT1 (for SIRT1, $EC_{1.5}$ = 2.7 μM; for SIRT1^{Q345A}, $EC_{1.5}$ = 12.2 μM). **20b** could only activate the enzymatic activity of SIRT1^{Q345A} by ∼2-fold at the highest dose. For SIRT1^{V445A}, approximately 2-fold change of $EC_{1.5}$ was observed (for SIRT1^{V445A}, $EC_{1.5}$ = 4.8 μM). **20b** could only activate the enzymatic activity of SIRT1^{V445A} by ∼3-fold. Furthermore, the kinetic parameters (K_m and V_{max}/K_m) of the fluorophore-peptide were determined in the absence or presence of **20b**, respectively. For SIRT1 wild-type, addition of **20b** resulted in a decrease of 135 μM of the K_m value (without **20b**, K_m = 240.4 μM; with **20b**, K_m = 104.8 μM), while for SIRT1^{Q345A} and SIRT1^{V445A}, the amount of K_m decrease reduced to 79 and 78 μM, respectively. Besides, after adding 10 μM of **20b**, the ratio of V_{max}/K_m significantly decreased after mutation of Gln 345 and Val 445 (for SIRT1, V_{max}/K_m = 13.1; for SIRT1^{Q345A}, V_{max}/K_m = 1.0; for SIRT1^{V445A}, V_{max}/K_m = 3.3). From the above analysis, we can see that for SIRT1^{Q345A} and SIRT1^{V445A} mutants, **20b** could not lower the K_m or increase V_{max}/K_m as much as that for the wild-type SIRT1. The mutants reduced the sensitivities to the compound, indicating that the side chains of Gln 345 and Val 445 take part in the interactions with **20b**.

Binding Mode of Imidazo[1,2-b]thiazole Derivatives. **4** and **5** belong to imidazo[1,2-*b*]thiazole derivatives. In 2009, the Sirtris group reported the activities of these derivatives with various amide groups.[23] In Table 6, we listed 13 compounds from the publication to discuss their SAR in combination with our model. As shown in Figure 7C, the piperazonomethyl fragment inserts into the cleft and forms van der Waals interactions with the loop on the large domain. The imidazo[2,1-*b*][1,3]thiazole group lies under the coumarin. The surfaces of the two aromatic fragments form a T-shaped stacking. **4** forms a bend at the phenyl group, and the trimethoxybenzene group forms a sandwich conformation with coumarin and arginine of the substrate.

In the publication by the Sirtris group, it is said that an aromatic group might be favorable at the R position because the cyclopentyl (**23**) and benzyl (**24**) exhibited low activities.[23] According to the binding mode of **4** (Figure 7C), the trimethoxyphenyl group forms $\pi-\pi$ interaction with the coumarin in which the aromatic substitutions at R position are indeed preferred. Substitution of methoxy groups at the benzene ring improved the activities as compared **4** and **25** to **27**. However, the low activity of **26** indicated that 2,4-dimethoxybenzene substitution is not well tolerated. A significant level of SIRT1 activation was observed if substituting the benzene ring (**27**) with monocyclic pyrimidine substitution (**28**). Furthermore, 2-substituted quinoline substitution (**29**) improved the potency in comparison with **4**, and 3-substituted quinoline substitution (**30**) was slightly more active than **29**. In like manner, introduction of heteroatoms such as nitrogen in the aromatic ring strengthened the stabilization of π-stacking. Notably, the 2-qunixaline group substitution (**5**) resulted in a significant increase of the activity. Besides, the activities of the compounds are highly dependent on the position of the heteroatom. For instance, different positions of the oxygen atom resulted in ∼10-fold change of $EC_{1.5}$ (**32** and **33**). This may be explained by the reason that the position of the heteroatom could induce different electron distributions of the π-cloud, which may affect the $\pi-\pi$ interaction between the compound and the fluorophore. Interestingly, changing the 2-quinoline group to the 8-quinoline group (**31**) led to a sharp loss of potency. In our model, the orientation of the 8-quinoline group is not favorable to form π-stacking with the coumarin.

Binding Mode of 1. Like compound **20b** and **4**, **1** was predicted to bind in the same site. As shown in Figure 7D, the 4-hydroxyphenyl ring of **1** and the coumarin are packed in "head-to-head" conformation; the *p*-hydroxyl may form H-bond with the coumarin. The histidine of the substrate is connected to Arg 446 on the large domain by 3,5-dihydroxyphenyl of **1** through H-bond. To validate the model, the mutagenesis studies were performed. **1** activated SIRT1 with an $EC_{1.5}$ of 23.6 μM and ∼8-fold enzymatic activity (Figure 2), which is consistent with previous studies.[44] We mutated Arg 446 to alanine, and the activation curve against the mutant was also determined (Supporting Information Figure S6). The maximum activation of **1** against SIRT1^{R446A} exhibited a significant decrease than that of the wild-type, with only ∼2-fold enhancement. Meanwhile, the $EC_{1.5}$ value decreased to 87.2 μM. Nevertheless, compound **20b** showed no difference in activating SIRT1 wild-type and SIRT1^{R446A} (Supporting Information Figure S6A). We assume that the side chain of Arg 446 may interact with **1** but not **20b**. For further validation, the kinetic parameters of ac-RHKK$_{ac}$-AMC against SIRT1 wild-type and mutant with or without **1** were determined. As shown in Table 5B, the K_m and V_{max}/K_m of the substrate for SIRT1 wild-type and SIRT1^{R446A} were similar; the mutation of the side chain did not change the binding affinity of the substrate. While in the presence of 50 μM **1**, the comparison of the kinetic parameters in wild-type (K_m = 111.3 μM, V_{max}/K_m = 11.4) and mutant (K_m = 134.3 μM, V_{max}/K_m = 4.4) indicated a reduced affinity of SIRT1 to the coumarin-labeled substrate. Notably, the ratio of V_{max}/K_m displayed about 3-fold decrease in the presence of **1** when the Arg 446 was mutated to alanine. The mutagenesis studies revealed that the side chain of Arg 446 interacted with the hydroxyl of **1**, and the binding was beneficial in the **1** activation.

On the basis of the above analysis, we may summarize the common features of the binding modes of the three SIRT1 activators. The aromatic portion of the SIRT1 activator forms π-stacking with the fluorophore. Heterocyclic or substituted aromatic compounds are preferred in the stacking, and SIRT1 activators with these fragments showed improved activities. Such observations were supported by the previous studies in π-stacking. It was reported that introduction of the heteroatom to benzene such as nitrogen could create a dipole and reduce the π-electron cloud in the spatial extent compared with benzene.[45−47] The substituted benzenes form stronger π-stacking than the unsubstituted ones.[48,49] Furthermore, the other portion of the activators may insert into the cleft under the fluorophore in a T-shaped stacking or in an extended conformation, which interact with residues from the large domain of SIRT1. The two portions of the activators may stabilize the substrate binding and promote the following catalysis. It is worth mentioning that the linker between the two portions is usually composed of 2−4 carbon/nitrogen atoms. The length of the linker is appropriate to allow the two

dx.doi.org/10.1021/jm301032j | J. Med. Chem. 2013, 56, 761−780

portions in the proper conformations to interact with the substrate or SIRT1 residues.

The Stability, Bioavailability, and Activity of Diaryl Acylhydrazone Derivatives in Cells. Apart from the above in vitro studies, we also tested the stability and bioavailability of our compound in cells. MCF-7 cells were treated with 100 μM **20b** and the cultured medium and cells were collected separately at different time points. Simultaneously, 100 μM **20b** was added to fresh medium to serve as control. In Figure 8,

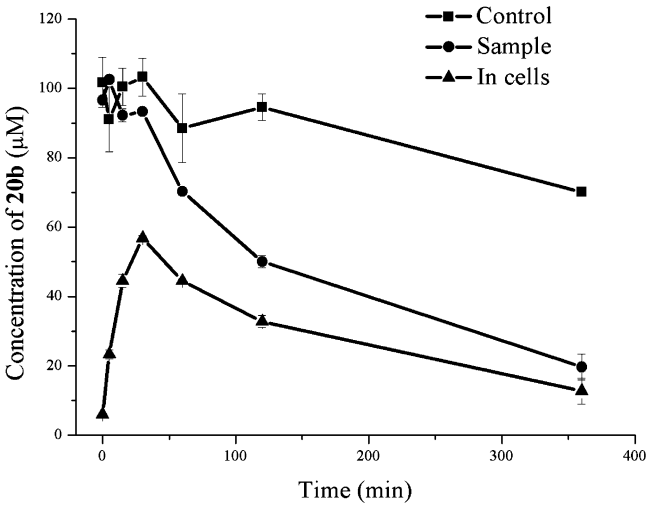

Figure 8. Stability test of compound **20b**. "Control" (squares) represents the amount of **20b** in fresh cell medium. "Sample" (circles) represents the total amount of **20b** in cultured medium and cells. "In cells" (triangles) represents the amount of **20b** in cells.

squares represent the concentrations of **20b** in fresh medium at different time points (Control). Circles represent the total amount of **20b** in cultured medium and cells (Sample). Triangles represent the amount of **20b** in cells (In cells). In comparison of the two curves (Control and Sample), **20b** remained stable in fresh medium for 120 min (squares), while in cultured medium the concentration of **20b** started to decrease after 30 min and it decreased to ~20 μM after 360 min in cell cultures (circles). These results indicated that the compound is stable in cells for a time period. As for the bioavailability, **20b** in cells achieved the maximum concentration at 30 min (triangles), at which over half of the compound could get into the cells.

Thus, the functional activity of our compound was further explored in a cell-based (MCF-7 cells) deacetylation assay.[22] In the experiment, p53 becomes acetylated at Lys 382 after DNA damage, which was induced by doxorubicin (DOX).[50] To determine the effect of compound **20b** on SIRT1 activity, trichostatin (TSA) was used to inhibit other classes of deacetylases. A reported SIRT1 activator, **1**, was used as control. As shown in Figure 9, **1** showed no effect on the acetyl-p53 level at the concentration lower than 100 μM. The acetyl-p53 level decreased along with the increase of the concentration of **1**. In the sample panel, the acetyl-p53 level decreased along with the increase amount of **20b**. However, no effect was detected when the concentration of **20b** decreased to 60 μM. The high concentrations of our compound used in the assay may be explained by the stability and bioavailability of the compound. In the Western blot, the cells were treated with the compounds for 6 h. The stability assay showed that the

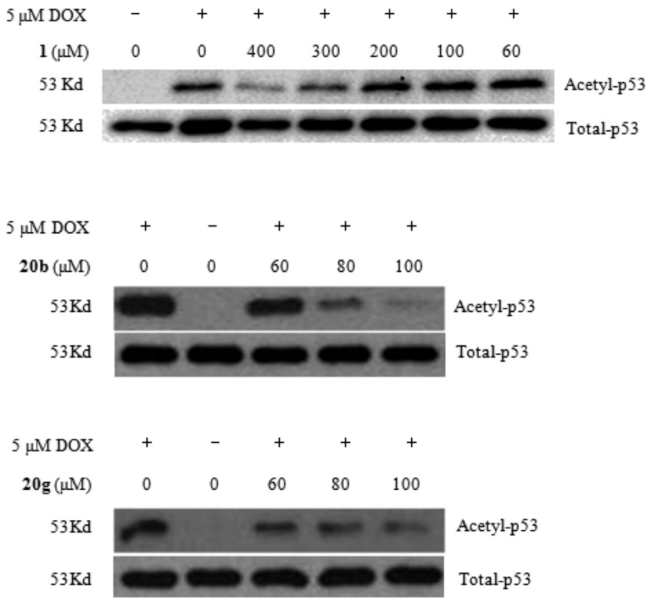

Figure 9. Western blot analysis of compounds **1**, **20b**, and **20g** on MCF-7 cells.

concentration of **20b** decreased from 100 to 20 μM after 6 h treatment in cells (Figure 8). In vitro, compound **20g** showed a comparable activation activity as **20b** (Table 3). Consistently, the Western blot results indicated that **20g** also decreased the acetyl-p53 on cell level (Figure 9). **20g** was slightly more effective than **20b**. Both **20b** and **20g** showed better activities than **1**.

Implications in the Discovery of Novel SIRT1 Activators. The aim of this study is to understand the structural basis by which the SIRT1 activators promote the deacetylation. The study revealed that the acceleration of the catalysis was dependent on the structural features of the substrates. For a specific acetyl substrate $(X_1 \cdots X_n)$-K_{ac}-Y, if residue Y comprises an aromatic ring, such as Phe, His, Tyr, or Trp, the steric bulk of Y would broaden the cleft of the catalysis domain as the fluorophore did and decrease the binding affinity of the substrate. In this case, SIRT1 activators may enhance the binding of substrate and accelerate the deacetylation. Studies by Dai et al. provided evidence to support the notion.[27] **4** was found to activate the deacetylation of ac-RHKK$_{ac}$-F-NH$_2$ and ac-RHKK$_{ac}$-W-NH$_2$ in a dose−response way but not on the substrate ac-RHKK$_{ac}$-A-NH$_2$.[27] However, in contrast with the inhibitory effect of **4** on ac-RHKK$_{ac}$-AMC reported by Dai et al., **4** was observed to activate the deacetylation of AMC-labeled peptide in our study. Thus, in search of SIRT1 activators for a specific substrate, the activation mechanism presented here may be broadly applicative. For instance, among the five acetylated lysine in human FOXO3,[7,51] three of the ε-acetylated lysines (Lys 259, Lys 290, and Lys 569) are followed by residues bearing aromatic rings (Tyr 260, Trp 291, and His 570). The reported SIRT1 activators may accelerate the deacetylation of native FOXO3. DNA methyltransferase 1(DNMT1) can be deacetylated by SIRT1 and a Phe is linked to the C-terminus of acetyl-Lys 1349,[52] and the reported compounds might also have activation effect on DNMT1. The substrate feature-dependent activation of SIRT1 activators may explain the controversial results due to the diversity of SIRT1 substrates.

In addition, the structure of "SIRT3/AcsCS2-K$_{ac}$" complex implicated that the binding of peptide induced the change of

dx.doi.org/10.1021/jm301032j | J. Med. Chem. 2013, 56, 761−780

protein conformation, and the conformational change is beneficial for the following catalysis. In light of the binding modes of the above three SIRT1 activators, one can design compounds which bind directly with the substrate and the residues around the peptide binding site, such as Phe 414 from the small domain and Arg 446 from the large domain (Figure 7). The small molecules targeting the binding site could link the two domains and decrease the K_m value of the substrate.

CONCLUSION

In this paper, we discovered a new class of small compounds that activate SIRT1 deacetylation activity by a fluorescence method. In the process of this project, it was reported that some putative activators did not directly bind to SIRT1. We then tried to understand the reason for the phenomenon. First, we determined the substrate selectivity of the diaryl acylhydrazone derivatives and **4** by HPLC. Through enzyme kinetics studies, **20b** and **4** were confirmed to decrease the K_m values of the fluorophore-labeled peptide, while none of them affected the unlabeled peptide. After that, we tried to capture the structure of the fluorophore-labeled peptide in the enzyme and determine the changes of enzyme conformation induced by the fluorophore. To our delight, the cocrystal structure of SIRT3 in complex with ac-RHKK$_{ac}$-AMC was obtained. In comparison with the structure of SIRT3 in complex with fluorophore-unlabeled peptide, the fluorophore was found to expand the substrate binding cleft and break the hydrogen bonds between the substrate and the loop on the Rossmann fold domain. A π-stacking of two coumarins were observed in a dimeric arrangement of the SIRT3 complexes. Our enzyme kinetics experiments and ITC data implied that the activators could be involved in π-stacking with the fluorophore. Computational analysis was then carried out to model the SIRT1 structure based on the "SIRT3/ac-RHKK$_{ac}$-AMC" complex structure and dock the small molecule activators into the SIRT1 model. The binding modes of **20b**, **1**, and **4** were consistent with the SAR and mutagenesis results.

Next, we put forward the activation mechanism of SIRT1 activators on the basis of the complex structures. For a SIRT1 activator, one portion of its structure forms π-stacking with the fluorophore of the substrate and the other portion may interact with the large domain of SIRT1. The small molecules link the substrate and the large domain together to compensate for the broadened cleft induced by the fluorophore and thus tighten the binding of the substrate. Moreover, we examined the activity, stability, and bioavailability of our compound in cells, which suggests that the compounds may be used as potentially interesting probes to study the functions of SIRT1. In summary, we elaborated the activation mechanism of the activators from the structural point. The complex structures and the mechanism described here provide the basis for development of novel SIRT1 activators and the studies of sirtuin activator activities in vivo and in vitro.

EXPERIMENTAL SECTION

Material. Unless otherwise noted, the reagents (chemicals) were purchased from commercial sources and used without further purification. Analytical thin layer chromatography (TLC) was performed on HSGF 254 (0.15−0.2 mm thickness). Compound spots were visualized by UV light (254 nm). Column chromatography was performed on silica gel FCP 200−300. Mircrowave reactions were carried on CEM reactor. Nuclear magnetic resonance (NMR) spectra were recorded on a Bruker AMX-300 NMR 300 or 400 MHz (TMS as IS). Chemical shifts were reported in parts per million (ppm, δ) downfield from tetramethylsilane. Proton coupling patterns are described as singlet (s), doublet (d), triplet (t), quartet (q), multiplet (m), and broad (br). Low- and high-resolution mass spectra (LRMS and HRMS) were obtained with electric, electrospray, and matrix-assisted laser desorption ionization (EI and ESI) produced by FinniganMAT-95 and LCQ-DECA spectrometers. HPLC analysis was conducted for all compounds listed in Tables 2−3 on an Agilent 1100 series HPLC with an Agilent Zorbax Eclipse XDB-C18 (4.6 mm × 50 mm, 5 μm) reversed phase column with two solvent systems (MeCN/H_2O/TFA and MeOH/H_2O/TFA). All the assayed compounds displayed a purity of 95−99% in both solvent systems.

General Procedure for Preparation of Esters 13a−k and 21h−i. A vial equipped with a magnetic stir bar was charged with $Pd(PPh_3)_4$ (0.05 mmol), KF·2H_2O (3.0 mmol), aryl bromide (1.0 mol), aryl boronic acid (1.2−1.5 mmol), and 4 mL of DME/H_2O/EtOH (7/3/2, v/v/v). Then the vial was capped with septa and heated at 110 °C for 50 min under microwave irradiation. The reaction mixture was extracted with EA. The organic layer was washed with brine, dried over anhydrous Na_2SO_4, and concentrated under vacuum. The crude product was purified by flash column chromatography to afford methyl esters **13a−k** and **21h−i**.

Methyl 4-[2-(Trifluoromethyl)phenyl]benzoate ***13a.*** Yield: 55%. ^{1}H NMR (400 MHz, $CDCl_3$) δ 8.10−8.06 (m, 2H), 7.76 (d, J = 8.0 Hz, 1H), 7. (t, J = 7.6 Hz, 1H), 7.51 (t, J = 7.6 Hz, 1H), 7.41 (d, J = 8.0 Hz, 2H), 7.32 (d, J = 7.6 Hz, 1H), 3.95 (s, 3H).

Methyl 4-(5-Cyano-2-hydroxyphenyl)benzoate ***13b.*** Yield: 36%. ^{1}H NMR (300 MHz, $CDCl_3$) δ 8.17 (d, J = 8.4 Hz, 2H), 7.61−7.52 (m, 4H), 7.06 (d, J = 9.0, 1H), 6.06 (br, 1H), 3.96 (s, 3H).

Methyl 4-(2H-1,3-Benzodioxol-5-yl)benzoate ***13c.*** Yield: 83%. ^{1}H NMR (300 MHz, $CDCl_3$) δ 8.07 (d, J = 8.4 Hz, 2H), 7.58 (d, J = 8.4 Hz, 2H), 7.13−7.08 (m, 2H), 6.90 (d, J = 8.7 Hz, 1H), 6.02 (s, 2H), 3.93 (s, 3H).

Methyl 3-Phenylbenzoate ***13d.*** Yield: 77%. ^{1}H NMR (300 MHz, $CDCl_3$) δ 8.29 (s, 1H), 8.02 (d, J = 7.8 Hz, 1H), 7.79 (d, J = 7.8 Hz, 1H), 7.63 (d, J = 7.2 Hz, 2H), 7.55−7.43 (m, 3H), 7.38 (t, J = 7.8 Hz, 1H), 3.95 (s, 3H).

Methyl 4-(Furan-2-yl)benzoate ***13h.*** Yield: 64%. ^{1}H NMR (300 MHz, $CDCl_3$) δ 8.05 (d, J = 8.4 Hz, 2H), 7.73 (d, J = 8.4 Hz, 2H), 7.52 (d, J = 1.8 Hz, 1H), 6.79 (d, J = 3.6 Hz, 1H), 6.51 (dd, J = 1.8, 3.6 Hz, 1H), 3.92 (s, 3H).

Methyl 4-(Pyridin-4-yl)benzoate ***13i.*** Yield: 79%. ^{1}H NMR (400 MHz, $CDCl_3$) δ 8.71 (d, J = 6.0 Hz, 2H), 8.16 (d, J = 8.4 Hz, 2H), 7.71 (d, J = 8.4 Hz, 2H), 7.56 (d, J = 6.0 Hz, 2H), 3.96 (s, 3H).

Methyl 4-(Pyridin-3-yl)benzoate ***13j.*** Yield: 68%. ^{1}H NMR (400 MHz, $CDCl_3$) δ 8.89 (d, J = 2.0 Hz, 1H), 8.65 (dd, J = 1.2, 4.8 Hz, 1H), 8.15 (d, J = 8.4 Hz, 2H), 7.95−7.92 (m, 1H), 7.69−7.63 (d, J = 8.4 Hz, 2H), 7.42 (dd, J = 4.8, 8.0 Hz, 1H), 3.95 (s, 3H).

Methyl 4-(Pyridin-2-yl)benzoate ***13k.*** Yield: 42%. ^{1}H NMR (400 MHz, $CDCl_3$) δ 8.89 (d, J = 2.0 Hz, 1H), 8.65 (dd, J = 1.2, 4.8 Hz, 1H), 8.15 (d, J = 8.4 Hz, 2H), 7.95−7.92 (m, 1H), 7.69−7.63 (d, J = 8.4 Hz, 2H), 7.42 (dd, J = 4.8, 8.0 Hz, 1H), 3.95 (s, 3H).

Methyl 6-(Furan-2-yl)naphthalene-2-carboxylate ***21h.*** Yield: 63%. ^{1}H NMR (300 MHz, DMSO-d_6) δ 8.62 (s, 1H), 8.30 (s, 1H), 8.18 (d, J = 8.7 Hz, 1H), 8.08 (d, J = 9.0 Hz, 1H), 8.01−7.96 (m, 2H), 7.87 (d, J = 1.5 Hz, 1H), 7.20 (d, J = 3.6 Hz, 1H), 6.69 (dd, J = 1.5, 3.3 Hz, 1H), 3.92 (s, 3H).

Methyl 6-Phenylnaphthalene-2-carboxylate ***21i.*** Yield: 53%. ^{1}H NMR (300 MHz, DMSO-d_6) δ 8.68 (s, 1H), 8.33 (s, 1H), 8.24 (d, J = 8.7 Hz, 1H), 8.12 (d, J = 8.7 Hz, 1H), 8.04−7.94 (m, 2H), 7.86 (d, J = 7.5 Hz, 2H), 7.54 (t, J = 7.5 Hz, 2H), 7.44 (t, J = 7.5 Hz, 1H), 3.93 (s, 3H).

6-Bromonaphthalene-2-carbohydrazide 19b. Representive Procedure for 14a−k, 19a−e, and 22h−i. To a solution of methyl 6-bromonaphthalene-2-carboxylate (513 mg, 1.94 mmol) in 9 mL of EtOH was added 3 mL of hydrazine hydrate (85%), and the resulting mixture was stirred under reflux for 3 h. After cooling to room temperature, the precipitate was filtered, washed with water, and dried to afford 6-bromonaphthalene-2-carbohydrazide as a white solid in 81% yield. ^{1}H NMR (300 MHz, DMSO-d_6) δ 9.95 (s, 1H), 8.44 (s,

dx.doi.org/10.1021/jm301032j | J. Med. Chem. 2013, 56, 761−780

1H), 8.28 (s, 1H), 8.03−7.94 (m, 3H), 7.71 (dd, J = 1.8, 8.7 Hz, 1H), 4.58 (s, 2H).

4-[2-(Trifluoromethyl)phenyl]benzohydrazide ***14a***. Yield: 75%. ^{1}H NMR (400 MHz, DMSO-d_6) δ 9.87 (s, 1H), 7.89−7.84 (m, 3H), 7.74 (t, J = 7.6 Hz, 1H), 7.64 (t, J = 7.6 Hz, 1H), 7.43−7.38 (m, 3H), 4.53 (s, 2H).

4-(5-Cyano-2-hydroxyphenyl)benzohydrazide ***14b***. Yield: 72%. ^{1}H NMR (400 MHz, DMSO-d_6) δ 10.94 (s, 1H), 9.82 (s, 1H), 7.86 (d, J = 8.4 Hz, 2H), 7.76 (d, J = 2.0 Hz, 1H), 7.69−7.63 (m, 3H), 7.10 (d, J = 8.4 Hz, 1H), 4.55 (s, 2H).

4-(2H-1,3-Benzodioxol-5-yl)benzohydrazide ***14c***. Yield: 78%. ^{1}H NMR (300 MHz, DMSO-d_6) δ 9.79 (s, 1H), 7.87 (d, J = 8.4 Hz, 2H), 7.68 (d, J = 8.4 Hz, 2H), 7.32 (d, J = 1.8 Hz, 1H), 7.22 (dd, J = 1.8, 8.1 Hz, 1H), 7.01 (d, J = 8.1 Hz, 1H), 6.07 (s, 2H), 4.54 (br, 2H).

3-Phenylbenzohydrazide ***14d***. Yield: 85%. ^{1}H NMR (400 MHz, DMSO-d_6) δ 9.89 (s, 1H), 8.10 (s, 1H), 7.81 (dd, J = 1.6, 7.6 Hz, 2H), 7.74 (d, J = 7.2 Hz, 2H), 7.56−7.48 (m, 3H), 7.40 (t, J = 7.6 Hz, 1H), 4.55 (s, 2H).

4-Phenylbenzohydrazide ***14e***. Yield: 88%. ^{1}H NMR (400 MHz, DMSO-d_6) δ 9.84 (s, 1H), 7.92 (d, J = 8.8 Hz, 2H), 7.76−7.71 (m, 4H), 7.49 (t, J = 7.6 Hz, 2H), 7.40 (t, J = 7.6 Hz, 1H), 4.52 (s, 2H).

4-(Furan-2-yl)benzohydrazide ***14h***. Yield: 82%. ^{1}H NMR (400 MHz, DMSO-d_6) δ 9.80 (s, 1H), 7.87 (d, J = 8.4 Hz, 2H), 7.81 (d, J = 0.8 Hz, 1H), 7.76 (d, J = 8.4 Hz, 2H), 7.09 (d, J = 3.6 Hz, 1H), 6.63 (dd, J = 1.6, 3.6 Hz, 1H), 4.53 (s, 2H).

4-(Pyridin-4-yl)benzohydrazide ***14i***. Yield: 74%. ^{1}H NMR (300 MHz, DMSO-d_6) δ 9.89 (s, 1H), 8.66 (dd, J = 1.5, 6.0 Hz, 2H), 7.97 (d, J = 8.4 Hz, 2H), 7.89 (d, J = 8.4 Hz, 2H), 7.76 (dd, J = 1.5, 6.0 Hz, 2H), 4.54 (s, 2H).

4-(Pyridin-3-yl)benzohydrazide ***14j***. Yield: 79%. ^{1}H NMR (400 MHz, DMSO-d_6) δ 9.87 (s, 1H), 8.95 (d, J = 2.0 Hz, 1H), 8.60 (dd, J = 2.0, 4.8 Hz, 1H), 8.17−8.11 (m, 1H), 7.95 (d, J = 8.4 Hz, 2H), 7.83 (d, J = 8.4 Hz, 2H), 7.51 (dd, J = 4.8, 7.2 Hz, 1H), 4.53 (s, 2H).

4-(Pyridin-2-yl)benzohydrazide ***14k***. Yield: 80%. ^{1}H NMR (400 MHz, DMSO-d_6) δ 9.87 (s, 1H), 8.69 (d, J = 4.8 Hz, 1H), 8.16 (d, J = 8.4 Hz, 2H), 8.04 (d, J = 8.0 Hz, 1H), 7.98−7.88 (m, 3H), 7.41−7.37 (m, 1H), 4.56 (s, 2H).

Quinoline-6-carbohydrazide ***19a***. Yield: 83%. ^{1}H NMR (400 MHz, DMSO-d_6) δ 10.01 (s, 1H), 8.97 (dd, J = 1.6, 4.0 Hz, 1H), 8.51−8.43 (m, 2H), 8.15 (dd, J = 1.6, 8.8 Hz, 1H), 8.06 (d, J = 8.8 Hz, 1H), 7.60 (dd, J = 4.0, 8.4 Hz, 1H), 4.68 (br, 2H).

6-Methanesulfonylnaphthalene-2-carbohydrazide ***19c***. Yield: 84%. ^{1}H NMR (300 MHz, DMSO-d_6) δ 10.06 (s, 1H), 8.64 (s, 1H), 8.56 (s, 1H), 8.30−8.26 (m, 2H), 8.07−7.99 (m, 2H), 4.68 (s, 2H).

6-Cyanonaphthalene-2-carbohydrazide ***19d***. Yield: 93%. ^{1}H NMR (300 MHz, DMSO-d_6) δ 10.06 (s, 1H), 8.64 (s, 1H), 8.52 (s, 1H), 8.21 (d, J = 8.4 Hz, 1H), 8.13 (d, J = 8.7 Hz, 1H), 8.04 (dd, J = 1.5, 8.4 Hz, 1H), 7.86 (dd, J = 1.5, 8.4 Hz, 1H), 4.63 (s, 2H).

6-Methoxynaphthalene-2-carbohydrazide ***19e***. Yield: 91%. ^{1}H NMR (300 MHz, DMSO-d_6) δ 9.82 (s, 1H), 8.35 (s, 1H), 7.91 (d, J = 9.0 Hz, 1H), 7.86 (s, 2H), 7.37 (d, J = 2.4 Hz, 1H), 7.22 (dd, J = 2.4, 9.0 Hz, 1H), 4.54 (br, 2H), 3.90 (s, 3H).

6-(Furan-2-yl)naphthalene-2-carbohydrazide ***22h***. Yield: 88%. ^{1}H NMR (300 MHz, DMSO-d_6) δ 9.93 (s, 1H), 8.40 (s, 1H), 8.26 (s, 1H), 8.06−8.00 (m, 2H), 7.95−7.89 (m, 2H), 7.85 (d, J = 1.5 Hz, 1H), 7.16 (d, J = 3.3 Hz, 1H), 6.67 (dd, J = 1.8, 3.3 Hz, 1H), 4.57 (s, 2H).

6-Phenylnaphthalene-2-carbohydrazide ***22i***. Yield: 84%. ^{1}H NMR (300 MHz, DMSO-d_6) δ 9.95 (s, 1H), 8.46 (s, 1H), 8.28 (s, 1H), 8.10 (d, J = 8.7 Hz, 1H), 8.05 (d, J = 10.0, Hz, 1H), 7.96−7.89 (m, 2H), 7.84 (d, J = 7.5 Hz, 2H), 7.53 (t, J = 7.5 Hz, 2H), 7.43 (t, J = 7.5 Hz, 1H), 4.57 (s, 2H).

6-Bromo-*N*′-(3,5-dibromo-2,4-dihydroxybenzylidene)-2-naphthohydrazide 20b. Representive Procedure for Compounds 16a−n and 20a−i. 6-Bromonaphthalene-2-carbohydrazide (100 mg, 0.38 mmol) and 3,5-dibromo-2,4-dihydroxybenzaldehyde (117 mg, 0.40 mmol) were suspended in 3 mL of EtOH/HAc (20/1, v/v). The resulting mixture was stirred for 3 h under reflux. The precipitate was collected by hot filtration and rinsed with EtOH to afford **20b** as a white solid in 72% yield. HPLC: 96.84%, t_R = 10.71. ^{1}H NMR (400 MHz, DMSO-d_6) δ 12.92 (s, 1H), 12.56 (s, 1H), 10.41 (br, 1H), 8.58 (s, 1H), 8.51 (s, 1H), 8.33 (s, 1H), 8.08−8.03 (m, 3H), 7.81−7.74 (m, 2H). EI-MS m/z (M^+) 540. EI-HRMS calcd for (M^+) 539.8320, found 539.8250.

N′*-(3,5-Dibromo-2,4-dihydroxybenzylidene)-2′-(trifluoromethyl)-biphenyl-4-carbohydrazide* ***16a***. Yield: 56%. HPLC: 99.28%, t_R = 10.18. ^{1}H NMR (400 MHz, DMSO-d_6) δ 12.91 (s, 1H), 12.45 (s, 1H), 10.41 (s, 1H), 8.49 (s, 1H), 8.00 (d, J = 8.4 Hz, 2H), 7.88 (d, J = 7.6 Hz, 1H), 7.80−7.75 (m, 2H), 7.67 (t, J = 7.8 Hz, 1H), 7.51 (d, J = 8.0 Hz, 2H), 7.46 (d, J = 7.6 Hz, 1H). EI-MS m/z (M^+) 556. EI-HRMS calcd for (M^+) 555.9245, found 555.9200.

4-(5-Cyano-2-hydroxyphenyl)-N′*-(3,5-dibromo-2,4-dihydroxybenzylidene)benzohydrazide* ***16b***. Yield: 62%. HPLC: 99.04%, t_R = 8.85. ^{1}H NMR (300 MHz, DMSO-d_6) δ 12.88 (s, 1H), 12.32 (s, 1H), 10.91 (s, 1H), 9.86 (br, 1H), 8.50 (s, 1H), 8.00 (d, J = 8.1 Hz, 2H), 7.81−7.73 (m, 4H), 7.67 (dd, J = 2.1, 8.4 Hz, 1H), 7.12 (d, J = 8.4 Hz, 1H). MS (ESI, m/z): 528.0 [M − H]$^-$. HRMS (ESI) calcd for $C_{21}H_{13}Br_2N_3O_4Na$ ([M + Na]$^+$) 551.9170; found 551.9160.

4-(Benzo[d][1,3]dioxol-5-yl)-N′*-(3,5-dibromo-2,4-dihydroxybenzylidene)benzohydrazide* ***16c***. Yield: 73%. HPLC: 96.09%, t_R = 6.89. ^{1}H NMR (300 MHz, DMSO-d_6) δ 12.94 (s, 1H), 12.38 (s, 1H), 10.42 (br, 1H), 8.48 (s, 1H), 8.00 (d, J = 8.1 Hz, 2H), 7.85−7.73 (m, 3H), 7.37 (s, 1H), 7.27 (d, J = 8.1 Hz, 1H), 7.04 (dd, J = 1.5, 8.1 Hz, 1H), 6.09 (s, 2H). MS (ESI, m/z): 533.0 [M + H]$^+$. HRMS (ESI) calcd for $C_{21}H_{13}Br_2N_2O_5$ ([M − H]$^-$) 530.9191; found 530.9186.

N′*-(3,5-Dibromo-2,4-dihydroxybenzylidene)biphenyl-3-carbohydrazide* ***16d***. Yield: 64%. HPLC: 95.70%, t_R = 23.56. ^{1}H NMR (400 MHz, DMSO-d_6) δ 12.91 (s, 1H), 12.42 (s, 1H), 10.41 (s, 1H), 8.49 (s, 1H), 8.20 (s, 1H), 7.96−7.90 (m, 2H), 7.79−7.74 (m, 3H), 7.65 (t, J = 7.6 Hz, 1H), 7.53 (t, J = 7.6 Hz, 2H), 7.43 (t, J = 7.2 Hz, 1H). MS (ESI, m/z): 489.2 [M + H]$^+$. HRMS (ESI) calcd for $C_{20}H_{14}Br_2N_2O_3Na$ ([M + H]$^+$) 510.9269; found 510.9280.

N′*-(2,4-Dihydroxybenzylidene)biphenyl-4-carbohydrazide* ***16e***. Yield: 33%. HPLC: 98.13%, t_R = 6.43. ^{1}H NMR (400 MHz, DMSO-d_6) δ 11.98 (s, 1H), 11.50 (s, 1H), 9.97 (s, 1H), 8.53 (s, 1H), 8.02 (d, J = 8.4 Hz, 2H), 7.85 (d, J = 8.4 Hz, 2H), 7.76 (d, J = 7.2 Hz, 2H), 7.51 (t, J = 7.6 Hz, 2H), 7.43 (t, J = 7.2 Hz, 1H), 7.32 (d, J = 8.4 Hz, 1H), 6.41−6.31 (m, 2H). EI-MS m/z (M^+) 332. EI-HRMS calcd for (M^+) 332.1161; found 332.1163.

N′*-(3,5-Dibromo-2-hydroxy-4-methoxybenzylidene)biphenyl-4-carbohydrazide* ***16f***. Yield: 78%. HPLC: 99.29%, t_R = 16.59. ^{1}H NMR (400 MHz, DMSO-d_6) δ 12.98 (s, 1H), 12.55 (s, 1H), 8.55 (s, 1H), 8.06 (d, J = 8.4 Hz, 2H), 7.91 (s, 1H), 7.87 (d, J = 8.4 Hz, 2H), 7.76 (d, J = 7.6 Hz, 2H), 7.51 (t, J = 7.6 Hz, 2H), 7.43 (t, J = 7.6 Hz, 1H), 3.83 (s, 3H). EI-MS m/z (M^+) 502. EI-HRMS calcd for (M^+) 501.9528; found 501.9501.

N′*-(3,5-Dibromo-4-hydroxy-2-methoxybenzylidene)biphenyl-4-carbohydrazide* ***16g***. Yield: 81%. HPLC: 96.32%, t_R = 6.32. ^{1}H NMR (400 MHz, DMSO-d_6) δ 11.99 (s, 1H), 8.61 (s, 1H), 8.08−8.00 (m, 3H), 7.84 (d, J = 8.4 Hz, 2H), 7.75 (d, J = 7.2 Hz, 2H), 7.51 (t, J = 7.2 Hz, 2H), 7.42 (t, J = 7.2 Hz, 1H), 3.83 (s, 3H). EI-MS m/z (M^+) 502. EI-HRMS calcd for (M^+) 501.9528; found 501.9524.

N′*-(3,5-Dibromo-2,4-dihydroxybenzylidene)-4-(furan-2-yl)-benzohydrazide* ***16h***. Yield: 55%. HPLC: 97.26%, t_R = 14.51. ^{1}H NMR (300 MHz, DMSO-d_6) δ 12.93 (s, 1H), 12.37 (s, 1H), 10.39 (s, 1H), 8.48 (s, 1H), 8.01 (d, J = 8.4 Hz, 2H), 7.90−7.83 (m, 3H), 7.77 (s, 1H), 7.16 (d, J = 3.6 Hz, 1H), 6.67 (dd, J = 1.8, 3.3 Hz, 1H). EI-MS m/z (M^+) 478. EI-HRMS calcd for (M^+) 477.9164; found 477.9148.

N′*-(3,5-Dibromo-2,4-dihydroxybenzylidene)-4-(pyridin-4-yl)-benzohydrazide* ***16i***. Yield: 71%. HPLC: 95.71%, t_R = 2.27. ^{1}H NMR (400 MHz, DMSO-d_6) δ 12.90 (s, 1H), 12.46 (s, 1H), 10.32 (s, 1H), 8.70 (d, J = 4.4 Hz, 2H), 8.50 (s, 1H), 8.10 (d, J = 8.4 Hz, 2H), 8.01 (d, J = 8.4 Hz, 2H), 7.83−7.77 (m, 3H). MS (ESI, m/z): 488.1 [M − H]$^-$. HRMS (ESI) calcd for $C_{19}H_{13}Br_2N_3O_3Na$ ([M + Na]$^+$) 511.9221; found 511.9240.

N′*-(3,5-Dibromo-2,4-dihydroxybenzylidene)-4-(pyridin-3-yl)-benzohydrazide* ***16j***. Yield: 63%. HPLC: 98.59%, t_R = 3.32. ^{1}H NMR (400 MHz, DMSO-d_6) δ 12.91 (s, 1H), 12.43 (s, 1H), 10.41 (s, 1H),

dx.doi.org/10.1021/jm301032j | J. Med. Chem. 2013, 56, 761−780

9.00 (d, J = 2.0 Hz 1H), 8.63 (d, J = 4.0 Hz, 1H), 8.50 (s, 1H), 8.23−8.16 (m, 1H), 8.08 (d, J = 8.4 Hz, 2H), 7.95 (d, J = 8.4 Hz, 2H), 7.78 (s, 1H), 7.54 (dd, J = 4.8, 8.0 Hz, 1H). MS (ESI, m/z): 490.1 [M + H]$^+$. HRMS (ESI) calcd for $C_{19}H_{14}Br_2N_3O_3$ ([M + H]$^+$) 489.9402; found 489.9391.

N′-(3,5-Dibromo-2,4-dihydroxybenzylidene)-4-(pyridin-2-yl)-benzohydrazide ***16k***. Yield: 65%. HPLC: 99.03%, t_R = 3.90. ^{1}H NMR (400 MHz, DMSO-d_6) δ 12.93 (s, 1H), 12.44 (s, 1H), 10.38 (s, 1H), 8.72 (d, J = 4.4 Hz, 1H), 8.50 (s, 1H), 8.27 (d, J = 8.0 Hz, 2H), 8.11−8.04 (m, 3H), 7.94 (t, J = 7.6 Hz, 1H), 7.78 (s, 1H), 7.45−7.40 (m, 1H). MS (ESI, m/z): 490.2 [M + H]$^+$. HRMS (ESI) calcd for $C_{19}H_{13}Br_2N_3O_3Na$ ([M + Na]$^+$) 511.9221; found 511.9221.

N′-(3,5-Dibromo-2,4-dihydroxybenzylidene)-4-methylbenzohydrazide ***16l***. Yield: 42%. HPLC: 98.90%, t_R = 9.18. ^{1}H NMR (400 MHz, DMSO-d_6) δ 12.94 (s, 1H), 12.26 (s, 1H), 10.39 (s, 1H), 8.45 (s, 1H), 7.85 (d, J = 8.0 Hz, 2H), 7.74 (s, 1H), 7.36 (d, J = 8.0 Hz, 2H), 2.39 (s, 3H). EI-MS m/z (M$^+$) 426. EI-HRMS calcd for (M$^+$) 425.9215; found 425.9213.

N′-(3,5-Dibromo-2,4-dihydroxybenzylidene)-4-(trifluoromethyl)-benzohydrazide ***16m***. Yield: 32%. HPLC: 98.94%, t_R = 13.82. ^{1}H NMR (300 MHz, DMSO-d_6) δ 12.79 (s, 1H), 12.54 (s, 1H), 10.43 (s, 1H), 8.49 (s, 1H), 8.14 (d, J = 8.1 Hz, 2H), 7.94 (d, J = 8.1 Hz, 2H), 7.80 (s, 1H). EI-MS m/z (M$^+$) 480. EI-HRMS calcd for (M$^+$) 479.8932; found 479.8916.

N′-(3,5-Dibromo-2,4-dihydroxybenzylidene)-3,5-dimethoxybenzohydrazide ***120b***. Yield: 54%. HPLC: 98.41%, t_R = 9.41. ^{1}H NMR (300 MHz, DMSO-d_6) δ 12.86 (s, 1H), 12.25 (s, 1H), 10.39 (s, 1H), 8.46 (s, 1H), 7.75 (s, 1H), 7.08 (d, J = 2.4 Hz, 2H), 6.74 (t, J = 2.4 Hz, 1H), 3.82 (s, 6H). MS (ESI, m/z): 471.1 [M − H]$^-$. HRMS (ESI) calcd for $C_{16}H_{14}Br_2N_2O_5Na$ ([M + Na]$^+$) 494.9167; found 494.9178.

N′-(3,5-Dibromo-2,4-dihydroxybenzylidene)quinoline-6-carbohydrazide ***20a***. Yield: 42%. HPLC: 97.19%, t_R = 3.59. ^{1}H NMR (300 MHz, DMSO-d_6) δ 12.89 (s, 1H), 12.59 (s, 1H), 10.41 (s, 1H), 9.04 (dd, J = 1.5, 4.2 Hz, 1H), 8.64 (d, J = 1.2 Hz, 1H), 8.60−8.51 (m, 2H), 8.26 (dd, J = 1.5, 8.4 Hz, 1H), 8.16 (d, J = 8.7 Hz, 1H), 7.80 (s, 1H), 7.67 (dd, J = 4.2, 8.1 Hz, 1H). MS (ESI, m/z): 462.0 [M − H]$^-$. HRMS (ESI) calcd for $C_{17}H_{11}Br_2N_3O_3Na$ ([M + Na]$^+$) 485.9065; found 485.9083.

6-Bromo-N′-(3,5-dibromo-2-hydroxy-4-methoxybenzylidene)-2-naphthohydrazide ***20c***. Yield: 79%. HPLC: 97.64%, t_R = 8.04. ^{1}H NMR (300 MHz, DMSO-d_6) δ 12.95 (s, 1H), 12.68 (s, 1H), 8.60 (s, 1H), 8.57 (s, 1H), 8.34 (d, J = 1.8 Hz 1H), 8.11−8.05 (m, 3H), 7.95 (s, 1H), 7.77 (dd, J = 1.8, 8.7 Hz, 1H), 3.84 (s, 3H). EI-MS m/z (M$^+$) 554. EI-HRMS calcd for (M$^+$) 553.8476; found 553.8457.

6-Bromo-N′-(3,5-dibromo-4-hydroxy-2-methoxybenzylidene)-2-naphthohydrazide ***20d***. Yield: 39%. HPLC: 95.16%, t_R = 8.59. ^{1}H NMR (300 MHz, DMSO-d_6) δ 12.12 (s, 1H), 10.56 (s, 1H), 8.62 (s, 1H), 8.57 (s, 1H), 8.33 (d, J = 1.2H, 1H), 8.09−8.00 (m, 4H), 7.76 (dd, J = 1.5, 8.7 Hz, 1H), 3.83 (s, 3H). EI-MS m/z (M$^+$) 554. EI-HRMS calcd for (M$^+$) 553.8476; found 553.8484.

N′-(3,5-Dibromo-2,4-dihydroxybenzylidene)-6-(methylsulfonyl)-2-naphthohydrazide ***20e***. Yield: 52%. HPLC: 96.63%, t_R = 5.64. ^{1}H NMR (300 MHz, DMSO-d_6) δ 12.89 (s, 1H), 12.65 (s, 1H), 10.44 (s, 1H), 8.70 (s, 2H), 8.53 (s, 1H), 8.39−8.33 (m, 2H), 8.15 (dd, J = 0.9, 9.3 Hz, 1H), 8.06 (dd, J = 1.5, 8.7 Hz, 1H), 7.82 (s, 1H), 3.3 (s, 3H). MS (ESI, m/z): 541.1 [M + H]$^+$. HRMS (ESI) calcd for $C_{19}H_{13}Br_2N_2O_5S$ ([M − H]$^-$) 538.8912; found 538.8919.

6-Cyano-N′-(3,5-dibromo-2,4-dihydroxybenzylidene)-2-naphthohydrazide ***20f***. Yield: 37%. HPLC: 95.79%, t_R = 10.50. ^{1}H NMR (300 MHz, DMSO-d_6) δ 12.88 (s, 1H), 12.63 (s, 1H), 10.46 (s, 1H), 8.68 (d, J = 9.3 Hz, 2H), 8.52 (s, 1H), 8.30 (d, J = 8.4 Hz, 1H), 8.23 (d, J = 8.4 Hz, 1H), 8.13 (d, J = 9.3 Hz, 1H), 7.92 (d, J = 8.7 Hz, 1H), 7.81 (s, 1H). MS (ESI, m/z): 486.1 [M − H]$^-$. HRMS (ESI) calcd for $C_{19}H_{11}Br_2N_3O_3Na$ ([M + Na]$^+$) 509.9065; found 509.9043.

N′-(3,5-Dibromo-2,4-dihydroxybenzylidene)-6-methoxy-2-naphthohydrazide ***20g***. Yield: 58%. HPLC: 95.11%, t_R = 16.07. ^{1}H NMR (300 MHz, DMSO-d_6) δ 13.00 (s, 1H), 12.45 (s, 1H), 10.39 (s, 1H), 8.50 (s, 2H), 8.00 (d, J = 9.0 Hz, 1H), 7.96 (s, 2H), 7.78 (s, 1H), 7.43 (d, J = 2.4 Hz, 1H), 7.28 (dd, J = 2.7, 9.0 Hz, 1H), 3.92 (s, 3H). MS (ESI, m/z): 491.2 [M − H]$^-$. HRMS (ESI) calcd for $C_{19}H_{14}Br_2N_2O_4Na$ ([M + Na]$^+$) 514.9218; found 514.9199.

N′-(3,5-Dibromo-2,4-dihydroxybenzylidene)-6-(furan-2-yl)-2-naphthohydrazide ***20h***. Yield: 67%. HPLC: 98.20%, t_R = 10.79. ^{1}H NMR (300 MHz, DMSO-d_6) δ 12.97 (s, 1H), 12.53 (s, 1H), 10.41 (s, 1H), 8.55 (d, J = 0.9 Hz, 1H), 8.52 (s, 1H), 8.31 (s, 1H), 8.13 (dd, J = 4.5, 8.7 Hz, 2H), 8.03−7.96 (m, 2H), 7.87 (dd, J = 0.6, 1.8 Hz, 1H), 7.80 (s, 1H), 7.20 (dd, J = 0.6, 3.3 Hz, 1H), 6.69 (dd, J = 1.8, 3.3 Hz, 1H). MS (ESI, m/z): 529.1 [M + H]$^+$. HRMS (ESI) calcd for $C_{22}H_{14}Br_2N_2O_4Na$ ([M + Na]$^+$) 550.9218; found 550.9246.

N′-(3,5-Dibromo-2,4-dihydroxybenzylidene)-6-phenyl-2-naphthohydrazide ***20i***. Yield: 91%. HPLC: 97.09%, t_R = 15.38. ^{1}H NMR (300 MHz, DMSO-d_6) δ 12.96 (s, 1H), 12.54 (s, 1H), 8.60 (s, 1H), 8.53 (s, 1H), 8.33 (s, 1H), 8.22−8.13 (m, 2H), 8.06−7.95 (m, 2H), 7.89−7.84 (m, 2H), 7.79 (s, 1H), 7.58−7.51 (m, 2H), 7.44 (t, J = 7.2 Hz, 1H). MS (ESI, m/z): 539.1 [M + H]$^+$. HRMS (ESI) calcd for $C_{24}H_{16}Br_2N_2O_3Na$ ([M + Na]$^+$) 560.9425; found 560.9414.

Protein Expression and Purification. DNA fragment which encodes SIRT1 (156−664) was inserted into pET28a vector (*Nde1*/*Xho1*) with a hexa histidine-tag at the N-terminal. The plasmid was transformed into *Escherichia coli* BL21 (DE3) competent cells. A single colony was inoculated in the LB medium with 50 μg/mL kanamycin at 37 °C. Then 500 μM IPTG was added to the cell culture when OD_{600} reached 0.8−1.0 and the protein was induced at 16 °C overnight. The cells were sonicated with SIRT1 lysis buffer (20 mM Tris, 200 mM NaCl, 5 mM β-ME, pH 8.0) and loaded to Ni-NTA. After washing with 40 mM imidazole, the protein was eluted with 500 mM imidazole. The elution was validated by SDS-PAGE and dialyzed into sirtuin deacetylation assay buffer in combination with glycerol (25 mM Tris, 137 mM NaCl, 2.7 mM KCl, 1 mM $MgCl_2$, 10% glycerol, pH 8.0). SIRT1^{Q345A}, SIRT1^{V445A}, and SIRT1^{R446A} plasmid were generated by site-directed mutagenesis kit (Stratagene, catalogue no 200518). The mutant was expressed and purified the same as the wild-type SIRT1.

DNA fragment which encodes SIRT3 (118−399) was inserted into pET21a vector (*BamH1*/*Xho1*) with a hexa histidine-tag at the N-terminal and a TEV cleavage site between the protein sequence and his-tag. The plasmid was transformed into *E. coli* BL21 (DE3) competent cells. A single colony was inoculated in the LB medium with 100 μg/mL ampicillin at 37 °C. Then 100 μM IPTG was added to the cell culture when OD_{600} reached 0.6−0.8 and the protein was induced at 16 °C overnight. The cells were sonicated with SIRT3 lysis buffer (25 mM Hepes, 200 mM NaCl, 5 mM β-ME, 5% glycerol, pH 7.5) and loaded to Ni-NTA. After washing with 40 mM imidazole, the protein was eluted with 250 mM imidazole. The elution was dialyzed into SIRT3 dialysis buffer (20 mM Tris, 200 mM NaCl, pH8.0) with TEV protease digestion at 4 °C overnight. The dialyzed protein was reloaded to Ni-NTA. The flow-through and 5 mM imizadole elution were collected and loaded to Superdex 200 (GE Healthcare) equilibrated with SIRT3 dialyze buffer. The peak representing SIRT3 monomer was collected and concentrated for crystallization.

DNA fragment which encodes SIRT2 (34−356) was inserted into pGET-4t-1 vector (*BamH1*/*EcoR1*) with a GST fusion protein at the N-terminus. The plasmid was transformed into *E. coli* BL21 (DE3) competent cells. A single colony was inoculated in the LB medium with 100 μg/mL ampicillin at 37 °C. Then 500 μM IPTG was added to the cell culture when OD_{600} reached 0.3 and the protein was induced at 37 °C for 5 h. The protein was purified by GST resin with SIRT1 lysis buffer and eluted with 10 mM GSH in SIRT1 lysis buffer. The elution was validated by SDS-PAGE and dialyzed the same as SIRT1 protein.

Screening of Sirtuin Activators and the $EC_{1.5}$ Determination of the Compounds. A fluorescent assay was used to screen the compounds against SIRT1, SIRT2, and SIRT3. The C-terminus of the acetyl peptide acetyl-Arg-His-Lys-Lys(ε-acetyl) was labeled with 4-amino-7-methylcoumarin. The ALY was deacetylated by sirtuins. Then, AMC could be cleaved from the peptide by trypsin. All compounds were dissolved in DMSO, and the screening concentration was fixed at 50 μM; compound **1** was used as control. For the compound screening against SIRT1, the reaction system contained 750 μM NAD$^+$, 31.25 μM ac-RHKK$_{ac}$-AMC, 1 μM SIRT1, and compounds/DMSO in sirtuin deacetylation assay buffer (25 mM Tris, 137 mM NaCl, 2.7 mM KCl, 1 mM $MgCl_2$, pH8.0). The reactions

dx.doi.org/10.1021/jm301032j | J. Med. Chem. 2013, 56, 761−780

were carried out at 25 °C for 45 min, stopped with 10 mM nicotinamide, and developed with 0.5 μg/μL trysin for 30 min. The fluorescence intensity of AMC was measured with a microplate reader (POLARstar OPTIMA, BMG Labtech); the excitation and emission wavelengths were set 340 and 490 nm. To examine the selectivity of the compounds, we tested the activity of the compounds on SIRT2 and SIRT3. The reaction conditions and procedures were the same as the screening assay on SIRT1 (750 μM of NAD^+, 31.25 μM of ac-$RHKK_{ac}$-AMC, 50 μM of compounds). To achieve the same enzymatic activity as SIRT1, the concentrations of SIRT2 and SIRT3 were 4.2 and 3.6 μM, respectively.

The $EC_{1.5}$ determination was carried out the same as the screening assay. Compounds were 3-fold diluted in DMSO and added to reaction system. $EC_{1.5}$ and maximum activation were calculated by fitting the data points with the dose−response function in Origin 8.0 (Origin lab).

Isothermal Titration Calorimetry. SIRT1 protein was dialyzed into sirtuin deacetylation assay buffer (25 mM Tris, 137 mM NaCl, 2.7 mM KCl, 1 mM $MgCl_2$, 5% glycerol, pH 8.0). The acetyl peptide was injected in 20 drops of 2 μL (the first drop was 0.5 μL and removed). The cell temperature was 26 °C, reference power was 5 μCal/s, initial delay was 60 s, and the stirring speed was 1000 rpm. All titrations were performed on a Microcal iTC200 (GE Healthcare). For the K_d detection of ac-$RHKK_{ac}$-NH_2 to SIRT1, 2.5 mM ac-$RHKK_{ac}$-NH_2 was titrated to 102 μM SIRT1. For the K_d detection of ac-$RHKK_{ac}$-AMC to SIRT1, 2.5 mM ac-$RHKK_{ac}$-AMC was titrated to 124 μM SIRT1. Raw data were integrated and analyzed with Origin 7.0 software (Origin lab). The data was fit to a one-site binding model.

Determination of K_m for Acetyl Peptide with or without AMC. *Fluorescent Assay.* To determine the K_m values of ac-$RHKK_{ac}$-AMC for SIRT1 wild-type and mutants in the absence and presence of compounds, the concentrations of NAD^+ and enzyme were fixed, with gradient concentration of peptide. DMSO was used as blank, and compounds were added as indicated. The procedures were the same as the above screening assay. The velocities were calculated by the discrepancies of fluorescence divided by time. The reciprocal data of velocities were plotted against the reciprocal data of peptide concentration, and the x intercept equals to negative $1/K_m$.

HPLC Assay. To determine the K_m values of ac-$RHKK_{ac}$-NH_2 in the absence and presence of compounds, SIRT1 was fixed at 1 μM and NAD^+ was fixed at 2 mM, the concentrations of ac-$RHKK_{ac}$-NH_2 were 1000, 500, 250, 125, 62.5, 31.25, 15.625, and 7.8125 μM, respectively. Indicated compounds were added to the reaction system (50 μM **4**, 10 μM compound **20b** or DMSO for blank). The reactions were carried out at 25 °C for 30 min and stopped by 10 mM nicotinamide. The K_m values of ac-$RHKK_{ac}$-AMC were determined in the same way as ac-$RHKK_{ac}$-NH_2 except that the concentrations of the peptide were set to 300, 150, 100, and 70 μM, respectively. After the reactions were stopped, the solution was centrifuged at 13000 rpm for 10 min, and the supernatant was transferred to glass vials for HPLC detection.

The reactions of ac-$RHKK_{ac}$-NH_2 were monitored by ultra performance liquid chromatography (UPLC). The separation was performed at 30 °C by using the Acquity UPLC BEH Shield RP 18 column (50 mm ×2.1 mm I.D., 1.7 μm) with the Waters Van Guard precolumn (5 mm × 2.1 mm I.D., 1.7 μm). The mobile phase consisted of buffer A (distilled water containing 0.1% TFA) and buffer B (acetonitrile containing 0.1% TFA) with a flow rate of 0.4 mL/min. The UV detection wavelength was set at 220 nm. The retention time of ac-$RHKK_{ac}$-NH_2 was 1.7 min (Supporting Information Figure S2A).

The reactions with ac-$RHKK_{ac}$-AMC were monitored by Dionex UltiMate 3000 HPLC system. The separation was achieved at 30 °C by using the Zorbax SB-Aq C18 column (250 mm × 4.6 mm I.D., 5 μm, Agilent Corp., USA) with the Alltima C18 guard column (5 mm × 4.6 mm I.D., 5 μm, Grace Corp., USA). The mobile phase was the same as above with a flow rate of 1 mL/min. The UV detection wavelength was set at 325 nm. The retention times of ac-RHKK-AMC and ac-$RHKK_{ac}$-AMC were 6 and 10.5 min, respectively (Supporting Information Figure S2B).

To determine the K_m values, the peak area of the remaining acetyl substrate was converted to molar concentration by using the peptide standard curve, and the deacetylated amount of substrate was determined. The velocities were calculated by the deacetylated amount of substrate divided by time. The calculation of K_m was the same as described above.

Crystallization, Data Collection, And Structure Determination. For "SIRT3/ac-$RHKK_{ac}$-AMC peptide" cocrystallization, the molar ratio of ac-$RHKK_{ac}$-AMC and SIRT3 protein was 1:1. SIRT3 was concentrated to 7 mg/mL, and the according amount of ac-$RHKK_{ac}$-AMC peptide powder was added to the protein. The mixture was incubated at 4 °C overnight and centrifuged for crystallization. The "SIRT3/ac-$RHKK_{ac}$-AMC" cocrystals were obtained by the hanging-drop vapor-diffusion method at 15 °C with crystallization solution containing 0.085 M Hepes-Na (pH 7.5), 8.5% (v/v) isopropyl alcohol, 17% (w/v) PEG 4000, and 15% (v/v) glycerol anhydrous.

The "SIRT3/ac-RHKKac-AMC" crystals were flash-frozen in liquid nitrogen. The diffraction data were collected on beamline BL17U at Shanghai Synchrotron Radiation Facility (SSRF) and processed by using HKL2000 program.[35] The space group of the complex was $R32$ with one "SIRT3/ac-$RHKK_{ac}$-AMC" complex in the asymmetric unit. The data set was reprocessed by Scalepack2mtz in the ccp4 suite,[36] and the structure was solved by MolRep[53] with apo-SIRT3 structure as the template (PDB ID: 3GLS). The structure refinement was carried out by Shelx97,[54] Refmac5,[55] and COOT.[56] The detailed information of diffraction data and refinement statistics were listed in Table 4.

Homology Modeling and Docking Simulation. The sequence of SIRT1 (244−498) was retrieved from the UniProt database (UniProtKB code: Q96EB6, http://www.uniprot.org/). SIRT1 model was built with the crystal structures of "SIRT3/ac-$RHKK_{ac}$-AMC" (SIRT3−121−157 and SIRT3−168−391) and "SIRT3/AcsCS2-K_{ac}" (SIRT3−158−167, PDB ID 3GLR) as templates. The sequences of SIRT1 and SIRT3 were aligned by ClustalW (Supporting Information Figure S4).[57] The aligned sequences were input into Discovery Studio (Accelrys) and SIRT1 model structure was built by the Build Homology module. The model of SIRT1 was further validated by Profiles-3D,[58] and the overall compatibility score of the model was 100.37, which was much higher than the expected low score 52.15. The Ramachandran plot revealed two residues (Leu 404 and Ala 405) in the disallowed region (Supporting Information Figure S7B), but the residues are far away from the peptide binding site. Therefore, the quality of SIRT1 model was acceptable for the following study. The model of SIRT1 was superimposed into the SIRT3 complex structure, and the coordinates of ac-$RHKK_{ac}$-AMC were copied from the complex structure to the SIRT1 model to build SIRT1/ac-$RHKK_{ac}$-AMC model.

The structures of compounds **20b**, **1**, and **4** were built with the Simulate Structure package in Discovery Studio. The structures were assigned with CHARm forcefield parameters and optimized by energy minimization. Autodock 4.2 was used to predict the binding modes of the compounds in SIRT1.[59] SIRT1/ac-$RHKK_{ac}$-AMC model structure was applied with CHARm forcefield. The mol2 files of compounds and the pdb file of protein were pretreated with AutoDock Tools 1.5.4.[60] In the docking procedure, the genetic algorithm (GA) was used. The number of GA runs was set to 50, population size was set to 200 and maximum number of top individuals that automatically survive was set to 2. The grid box was centered at the substrate binding cleft under the fluorophore. Other parameters were set as default. After running autogrid and autodock, the possible poses of compounds in SIRT1 were obtained.

Stability Test. The stability of compound **20b** was tested on human breast cancer cells MCF-7. The cells were treated with **20b** for 0, 5, 15, 30, 60, 120, and 360 min. The medium was removed at the end point, and equal volume of acetonitrile was added. Cells were washed and treated with acetonitrile. The medium and cell lysate were collected separately for detection. **20b** was added to absolute cell medium and treated the same to serve as control. The samples were centrifuged and injected onto the Agilent 1260 Infinity HPLC system (Agilent Technologies, Waldbronn, Germany). Separation was achieved using a Hypersil GOLD Dim column (100 mm × 4.6 mm I.D., 3 μm; Thermo Fisher Scientific, Runcorn, Cheshire, UK) at a flow rate of 1 mL/min. The column was maintained at room

temperature. A mobile phase of acetonitrile−5 mM ammonium acetate−formic acid (50:50:0.1, v/v/v) was employed. The effluent was monitored via ultraviolet detection at 340 nm.

Western Blotting. Human cancer cell line MCF-7 cells were seeded at a density of 1×10^5 in 6-well plates with Dulbecco's Modified Eagle's Medium (DMEM) plus 10% fetal calf serum. Cells were incubated in a humidified atmosphere containing 5% CO_2 at 37 °C for 24 h. Gradient concentrations of **1**, **20b**, or **20g** plus 0.1 μM TSA and 5 μM DOX were added to MCF-7 cells. After incubation for 6 h, cells were collected and lysed by using a kit from Active Motif (Carlsbad, CA). Total protein concentration was determined by BCA kit (catalogue no. P0012, Beyotime Institute of Biotechnology, Shanghai, China). Samples containing 50 μg of protein were loaded onto a 9% gel. The proteins were transferred to a nitrocellulose membrane (Whatman, UK) after electrophoresis. Then 5% nonfat milk in TBST (10 mM Tris pH7.5, 150 mM NaCl, 0.05% Tween-20) was used to block the nonspecific reactivity. To determine the acetyl-p53, the membrane was incubated with polyclonal antibody against acetyl-p53 (Cell Signaling Technology, catalogue no. 2525) at 4 °C overnight. Immune complexes were detected with horseradish peroxidase-conjugated goat antirabbit IgG antibody and visualized with a SuperSignal West Dura Kit (Pierce). To determine the total p53, the same blot was reprobed and p53 antibody (Cell Signaling Technology, catalogue no. 2527) was used.

■ ASSOCIATED CONTENT

Ⓢ Supporting Information

Information about the synthesis of the chemical compounds, molecular modeling, HPLC data, isothermal titration calorimetry, enzyme kinetics data, etc. This material is available free of charge via the Internet at http://pubs.acs.org.

Accession Codes

The coordinates of "SIRT3/ac-RHKK$_{ac}$-AMC" complex structure were deposited in protein data bank with the PDB ID of 4FZ3.

■ AUTHOR INFORMATION

Corresponding Author

*For D.L.: E-mail: dxl@mail.shcnc.ac.cn. For H.L.: phone, +86-21-50806600; fax, +86-21-50807088; E-mail, hliu@mail.shcnc.ac.cn.

Present Address

¶Shanghai Institute of Materia Medica, Chinese Academy of Sciences, 555 Zu-Chong-Zhi Road, Shanghai 201203, China

Author Contributions

▽These authors contributed equally to this work.

Notes

The authors declare no competing financial interest.

■ ACKNOWLEDGMENTS

We thank Prof. Tony Kouzarides for kindly providing the plasmid of SIRT1, Prof. Anita Büttner for kindly providing the plasmid of SIRT2, and Prof. Clemens Steegborn for kindly providing the plasmid of SIRT3. The work was supported by the National Science Fund (grant 21021063, grant 91229204) and the Science and Technology Commission of Shanghai Municipality (grant 08JC1422100).

■ ABBREVIATIONS USED

KDAC, lysine deacetylase; NAD^+, nicotinamide adenine dinucleotide; PPARγ, peroxisome proliferator activated receptor γ; FOXO, forkhead homeobox type O; BESTO, β cell-specific SIRT1-overexpressing; Ucp2, uncoupling protein 2; PGC-1α, peroxisome proliferator activated receptor gamma coactivator 1; SAR, structure−activity relationship; AMC, 4-amino-7-methylcoumarin; ITC, isothermal titration calorimetry; ALY, acetyl-lysine; DNMT1, DNA methyltransferase 1; DOX, doxorubicin; TSA, trichostatin

■ REFERENCES

(1) Landry, J.; Sutton, A.; Tafrov, S. T.; Heller, R. C.; Stebbins, J.; Pillus, L.; Sternglanz, R. The silencing protein SIR2 and its homologs are NAD-dependent protein deacetylases. *Proc. Natl. Acad. Sci. U. S. A.* **2000**, *97*, 5807−5811.

(2) North, B. J.; Verdin, E. Sirtuins: Sir2-related NAD-dependent protein deacetylases. *Genome Biol.* **2004**, *5*, 224−236.

(3) Vaquero, A.; Scher, M.; Lee, D. H.; Erdjument-Bromage, H.; Tempst, P.; Reinberg, D. Human SirT1 interacts with histone H1 and promotes formation of facultative heterochromatin. *Mol. Cell* **2004**, *16*, 93−105.

(4) Vaquero, A.; Sternglanz, R.; Reinberg, D. NAD^+-dependent deacetylation of H4 lysine 16 by class III HDACs. *Oncogene* **2007**, *26*, 5505−5520.

(5) Picard, F.; Kurtev, M.; Chung, N.; Topark-Ngarm, A.; Senawong, T.; Machado De Oliveira, R.; Leid, M.; McBurney, M. W.; Guarente, L. Sirt1 promotes fat mobilization in white adipocytes by repressing PPAR-gamma. *Nature* **2004**, *429*, 771−776.

(6) Qiao, L. P.; Shao, J. H. SIRT1 regulates adiponectin gene expression through Foxo1-C/enhancer-binding protein alpha transcriptional complex. *J. Biol. Chem.* **2006**, *281*, 39915−39924.

(7) Brunet, A.; Sweeney, L. B.; Sturgill, J. F.; Chua, K. F.; Greer, P. L.; Lin, Y.; Tran, H.; Ross, S. E.; Mostoslavsky, R.; Cohen, H. Y.; Hu, L. S.; Cheng, H. L.; Jedrychowski, M. P.; Gygi, S. P.; Sinclair, D. A.; Alt, F. W.; Greenberg, M. E. Stress-dependent regulation of FOXO transcription factors by the SIRT1 deacetylase. *Science* **2004**, *303*, 2011−2015.

(8) Bordone, L.; Motta, M. C.; Picard, F.; Robinson, A.; Jhala, U. S.; Apfeld, J.; McDonagh, T.; Lemieux, M.; McBurney, M.; Szilvasi, A.; Easlon, E. J.; Lin, S. J.; Guarente, L. Sirt1 regulates insulin secretion by repressing UCP2 in pancreatic beta cells. *PLoS Biol.* **2006**, *4*, 210−220.

(9) Ramsey, K. M.; Mills, K. F.; Satoh, A.; Imai, S. I. Age-associated loss of Sirt1-mediated enhancement of glucose-stimulated insulin secretion in beta cell-specific Sirt1-overexpressing (BESTO) mice. *Aging Cell* **2008**, *7*, 78−88.

(10) Rodgers, J. T.; Lerin, C.; Haas, W.; Gygi, S. P.; Spiegelman, B. M.; Puigserver, P. Nutrient control of glucose homeostasis through a complex of PGC-1alpha and SIRT1. *Nature* **2005**, *434*, 113−118.

(11) Lagouge, M.; Argmann, C.; Gerhart-Hines, Z.; Meziane, H.; Lerin, C.; Daussin, F.; Messadeq, N.; Milne, J.; Lambert, P.; Elliott, P.; Geny, B.; Laakso, M.; Puigserver, P.; Auwerx, J. Resveratrol improves mitochondrial function and protects against metabolic disease by activating SIRT1 and PGC-1 alpha. *Cell* **2006**, *127*, 1109−1122.

(12) Blander, G.; Guarente, L. The sir2 family of protein deacetylases. *Annu. Rev. Biochem.* **2004**, *73*, 417−435.

(13) Longo, V. D.; Kennedy, B. K. Sirtuins in aging and age-related disease. *Cell* **2006**, *126*, 257−268.

(14) Howitz, K. T.; Bitterman, K. J.; Cohen, H. Y.; Lamming, D. W.; Lavu, S.; Wood, J. G.; Zipkin, R. E.; Chung, P.; Kisielewski, A.; Zhang, L.-L.; Scherer, B.; Sinclair, D. A. Small molecule activators of sirtuins extend *Saccharomyces cerevisiae* lifespan. *Nature* **2003**, *425*, 191−196.

(15) Wood, J. G.; Rogina, B.; Lavu, S.; Howitz, K.; Helfand, S. L.; Tatar, M.; Sinclair, D. Sirtuin activators mimic caloric restriction and delay ageing in metazoans. *Nature* **2004**, *430*, 686−689.

(16) Bauer, J. H.; Goupil, S.; Garber, G. B.; Helfand, S. L. An accelerated assay for the identification of lifespan-extending interventions in *Drosophila melanogaster*. *Proc. Natl. Acad. Sci. U. S. A.* **2004**, *101*, 12980−12985.

(17) Valenzano, D. R.; Terzibasi, E.; Genade, T.; Cattaneo, A.; Domenici, L.; Cellerino, A. Resveratrol prolongs lifespan and retards the onset of age-related markers in a short-lived vertebrate. *Curr. Biol.* **2006**, *16*, 296−300.

(18) Sun, C.; Zhang, F.; Ge, X. J.; Yan, T. T.; Chen, X. M.; Shi, X. L.; Zhai, Q. W. SIRT1 improves insulin sensitivity under insulin-resistant conditions by repressing PTP1B. *Cell Metab.* **2007**, *6*, 307−319.
(19) Csiszar, A.; Labinskyy, N.; Pinto, J. T.; Ballabh, P.; Zhang, H.; Losonczy, G.; Pearson, K.; de Cabo, R.; Pacher, P.; Zhang, C.; Ungvari, Z. Resveratrol induces mitochondrial biogenesis in endothelial cells. *Am. J. Physiol.: Heart Circ. Physiol.* **2009**, *297*, 13−20.
(20) Nayagam, V. M.; Wang, X.; Tan, Y. C.; Poulsen, A.; Goh, K. C.; Ng, T.; Wang, H.; Song, H. Y.; Ni, B.; Entzeroth, M.; Stunkel, W. SIRT1 modulating compounds from high-throughput screening as anti-inflammatory and insulin-sensitizing agents. *J. Biomol. Screening* **2006**, *11*, 959−967.
(21) Mai, A.; Valente, S.; Meade, S.; Carafa, V.; Tardugno, M.; Nebbioso, A.; Galmozzi, A.; Mitro, N.; De Fabiani, E.; Altucci, L.; Kazantsev, A. Study of 1,4-dihydropyridine structural scaffold: discovery of novel sirtuin activators and inhibitors. *J. Med. Chem.* **2009**, *52*, 5496−5504.
(22) Milne, J. C.; Lambert, P. D.; Schenk, S.; Carney, D. P.; Smith, J. J.; Gagne, D. J.; Jin, L.; Boss, O.; Perni, R. B.; Vu, C. B.; Bemis, J. E.; Xie, R.; Disch, J. S.; Ng, P. Y.; Nunes, J. J.; Lynch, A. V.; Yang, H.; Galonek, H.; Israelian, K.; Choy, W.; Iffland, A.; Lavu, S.; Medvedik, O.; Sinclair, D. A.; Olefsky, J. M.; Jirousek, M. R.; Elliott, P. J.; Westphal, C. H. Small molecule activators of SIRT1 as therapeutics for the treatment of type 2 diabetes. *Nature* **2007**, *450*, 712−716.
(23) Vu, C. B.; Bemis, J. E.; Disch, J. S.; Ng, P. Y.; Nunes, J. J.; Milne, J. C.; Carney, D. P.; Lynch, A. V.; Smith, J. J.; Lavu, S.; Lambert, P. D.; Gagne, D. J.; Jirousek, M. R.; Schenk, S.; Olefsky, J. M.; Perni, R. B. Discovery of imidazo[1,2-*b*]thiazole derivatives as novel SIRT1 activators. *J. Med. Chem.* **2009**, *52*, 1275−1283.
(24) Bemis, J. E.; Vu, C. B.; Xie, R.; Nunes, J. J.; Ng, P. Y.; Disch, J. S.; Milne, J. C.; Carney, D. P.; Lynch, A. V.; Jin, L.; Smith, J. J.; Lavu, S.; Iffland, A.; Jirousek, M. R.; Perni, R. B. Discovery of oxazolo[4,5-*b*]pyridines and related heterocyclic analogs as novel SIRT1 activators. *Bioorg. Med. Chem. Lett.* **2009**, *19*, 2350−2353.
(25) Kaeberlein, M.; McDonagh, T.; Heltweg, B.; Hixon, J.; Westman, E. A.; Caldwell, S. D.; Napper, A.; Curtis, R.; DiStefano, P. S.; Fields, S.; Bedalov, A.; Kennedy, B. K. Substrate-specific activation of sirtuins by resveratrol. *J. Biol. Chem.* **2005**, *280*, 17038−17045.
(26) Pacholec, M.; Bleasdale, J. E.; Chrunyk, B.; Cunningham, D.; Flynn, D.; Garofalo, R. S.; Griffith, D.; Griffor, M.; Loulakis, P.; Pabst, B.; Qiu, X.; Stockman, B.; Thanabal, V.; Varghese, A.; Ward, J.; Withka, J.; Ahn, K. SRT1720, SRT2183, SRT1460, and resveratrol are not direct activators of SIRT1. *J. Biol. Chem.* **2010**, *285*, 8340−8351.
(27) Dai, H.; Kustigian, L.; Carney, D.; Case, A.; Considine, T.; Hubbard, B. P.; Perni, R. B.; Riera, T. V.; Szczepankiewicz, B.; Vlasuk, G. P.; Stein, R. L. SIRT1 activation by small molecules: kinetic and biophysical evidence for direct interaction of enzyme and activator. *J. Biol. Chem.* **2010**, *285*, 32695−32703.
(28) Bass, T. M.; Weinkove, D.; Houthoofd, K.; Gems, D.; Partridge, L. Effects of resveratrol on lifespan in *Drosophila melanogaster* and *Caenorhabditis elegans*. *Mech. Ageing Dev.* **2007**, *128*, 546−552.
(29) Feige, J. N.; Lagouge, M.; Canto, C.; Strehle, A.; Houten, S. M.; Milne, J. C.; Lambert, P. D.; Mataki, C.; Elliott, P. J.; Auwerx, J. Specific SIRT1 activation mimics low energy levels and protects against diet-induced metabolic disorders by enhancing fat oxidation. *Cell Metab.* **2008**, *8*, 347−358.
(30) Smith, J. J.; Kenney, R. D.; Gagne, D. J.; Frushour, B. P.; Ladd, W.; Galonek, H. L.; Israelian, K.; Song, J.; Razvadauskaite, G.; Lynch, A. V.; Carney, D. P.; Johnson, R. J.; Lavu, S.; Iffland, A.; Elliott, P. J.; Lambert, P. D.; Elliston, K. O.; Jirousek, M. R.; Milne, J. C.; Boss, O. Small molecule activators of SIRT1 replicate signaling pathways triggered by calorie restriction in vivo. *BMC Syst. Biol.* **2009**, *3*, 31−45.
(31) He, L.; Zhang, L.; Liu, X.; Li, X.; Zheng, M.; Li, H.; Yu, K.; Chen, K.; Shen, X.; Jiang, H.; Liu, H. Discovering potent inhibitors against the beta-hydroxyacyl-acyl carrier protein dehydratase (FabZ) of *Helicobacter pylori*: structure-based design, synthesis, bioassay, and crystal structure determination. *J. Med. Chem.* **2009**, *52*, 2465−2481.
(32) Boehlow, T. R.; Harburn, J. J.; Spilling, C. D. Approaches to the synthesis of some tyrosine-derived marine sponge metabolites: synthesis of verongamine and purealidin N. *J. Org. Chem.* **2001**, *66*, 3111−3118.
(33) Napper, A. D.; Hixon, J.; McDonagh, T.; Keavey, K.; Pons, J. F.; Barker, J.; Yau, W. T.; Amouzegh, P.; Flegg, A.; Hamelin, E.; Thomas, R. J.; Kates, M.; Jones, S.; Navia, M. A.; Saunders, J. O.; DiStefano, P. S.; Curtis, R. Discovery of indoles as potent and selective inhibitors of the deacetylase SIRT1. *J. Med. Chem.* **2005**, *48*, 8045−8054.
(34) Sanders, B. D.; Jackson, B.; Marmorstein, R. Structural basis for sirtuin function: what we know and what we don't. *Biochim. Biophys. Acta, Proteins Proteomics* **2010**, *1804*, 1604−1616.
(35) Otwinowski, Z.; Minor, W. Processing of X-ray diffraction data collected in oscillation mode. *Macromol. Crystallogr., Part A* **1997**, *276*, 307−326.
(36) Collaborative computational project, number 4. The CCP4 suite: programs for protein crystallography. *Acta. Crystallogr., Sect. D: Biol. Crystallogr.* **1994**, *50*, 760−763.
(37) Sauve, A. A.; Celic, I.; Avalos, J.; Deng, H.; Boeke, J. D.; Schramm, V. L. Chemistry of gene silencing: the mechanism of NAD^+-dependent deacetylation reactions. *Biochemistry* **2001**, *40*, 15456−15463.
(38) Smith, B. C.; Denu, J. M. Sir2 protein deacetylases: evidence for chemical intermediates and functions of a conserved histidine. *Biochemistry* **2006**, *45*, 272−282.
(39) Jackson, M. D.; Schmidt, M. T.; Oppenheimer, N. J.; Denu, J. M. Mechanism of nicotinamide inhibition and transglycosidation by Sir2 histone/protein deacetylases. *J. Biol. Chem.* **2003**, *278*, 50985−50998.
(40) Jin, L.; Wei, W.; Jiang, Y.; Peng, H.; Cai, J.; Mao, C.; Dai, H.; Choy, W.; Bemis, J. E.; Jirousek, M. R.; Milne, J. C.; Westphal, C. H.; Perni, R. B. Crystal structures of human SIRT3 displaying substrate-induced conformational changes. *J. Biol. Chem.* **2009**, *284*, 24394−24405.
(41) Avalos, J. L.; Bever, K. M.; Wolberger, C. Mechanism of sirtuin inhibition by nicotinamide: altering the NAD^+ cosubstrate specificity of a Sir2 enzyme. *Mol. Cell* **2005**, *17*, 855−868.
(42) Min, J.; Landry, J.; Sternglanz, R.; Xu, R. M. Crystal structure of a SIR2 homolog−NAD complex. *Cell* **2001**, *105*, 269−279.
(43) Avalos, J. L.; Boeke, J. D.; Wolberger, C. Structural basis for the mechanism and regulation of Sir2 enzymes. *Mol. Cell* **2004**, *13*, 639−648.
(44) Borra, M. T.; Smith, B. C.; Denu, J. M. Mechanism of human SIRT1 activation by resveratrol. *J. Biol. Chem.* **2005**, *280*, 17187−17195.
(45) Geronimo, I.; Lee, E. C.; Singh, N. J.; Kim, K. S. How different are electron-rich and electron-deficient pi interactions? *J. Chem. Theory Comput.* **2010**, *6*, 1931−1934.
(46) Mishra, B. K.; Sathyamurthy, N. Pi−pi interaction in pyridine. *J. Phys. Chem. A* **2005**, *109*, 6−8.
(47) Mishra, B. K.; Sathyamurthy, N. Stacking interaction in pyrazine dimer. *J. Theor. Comput. Chem.* **2006**, *5*, 609−619.
(48) Lee, E. C.; Kim, D.; Jurecka, P.; Tarakeshwar, P.; Hobza, P.; Kim, K. S. Understanding of assembly phenomena by aromatic−aromatic interactions: benzene dimer and the substituted systems. *J. Phys. Chem. A* **2007**, *111*, 3446−3457.
(49) Sinnokrot, M. O.; Sherrill, C. D. Substituent effects in pi−pi interactions: sandwich and T-shaped configurations. *J. Am. Chem. Soc.* **2004**, *126*, 7690−7697.
(50) Sakaguchi, K.; Herrera, J. E.; Saito, S.; Miki, T.; Bustin, M.; Vassilev, A.; Anderson, C. W.; Appella, E. DNA damage activates p53 through a phosphorylation−acetylation cascade. *Genes Dev.* **1998**, *12*, 2831−2841.
(51) Wang, F.; Chan, C. H.; Chen, K.; Guan, X.; Lin, H. K.; Tong, Q. Deacetylation of FOXO3 by SIRT1 or SIRT2 leads to Skp2-mediated FOXO3 ubiquitination and degradation. *Oncogene* **2012**, *31*, 1546−1557.
(52) Peng, L.; Yuan, Z.; Ling, H.; Fukasawa, K.; Robertson, K.; Olashaw, N.; Koomen, J.; Chen, J.; Lane, W. S.; Seto, E. SIRT1

deacetylates the DNA methyltransferase 1 (DNMT1) protein and alters its activities. *Mol. Cell. Biol.* **2011**, *31*, 4720−4734.
(53) Vagin, A.; Teplyakov, A. MOLREP: an automated program for molecular replacement. *J. Appl. Crystallogr.* **1997**, *30*, 1022−1025.
(54) Sheldrick, G. M. A short history of SHELX. *Acta Crystallogr., Sect. A: Found. Crystallogr.* **2008**, *64*, 112−122.
(55) Vagin, A. A.; Steiner, R. A.; Lebedev, A. A.; Potterton, L.; McNicholas, S.; Long, F.; Murshudov, G. N. REFMAC5 dictionary: organization of prior chemical knowledge and guidelines for its use. *Acta Crystallogr., Sect. D: Biol. Crystallogr.* **2004**, *60*, 2184−2195.
(56) Emsley, P.; Cowtan, K. Coot: model-building tools for molecular graphics. *Acta Crystallogr., Sect. D: Biol. Crystallogr.* **2004**, *60*, 2126−2132.
(57) Thompson, J. D.; Higgins, D. G.; Gibson, T. J. Clustal-W improving the sensitivity of progressive multiple sequence alignment through sequence weighting, position-specific gap penalties and weight matrix choice. *Nucleic Acids Res.* **1994**, *22*, 4673−4680.
(58) Bowie, J. U.; Luthy, R.; Eisenberg, D. A method to identify protein sequences that fold into a known three-dimensional structure. *Science* **1991**, *253*, 164−170.
(59) Morris, G. M.; Goodsell, D. S.; Halliday, R. S.; Huey, R.; Hart, W. E.; Belew, R. K.; Olson, A. J. Automated docking using a Lamarckian genetic algorithm and an empirical binding free energy function. *J. Comput. Chem.* **1998**, *19*, 1639−1662.
(60) Morris, G. M.; Huey, R.; Lindstrom, W.; Sanner, M. F.; Belew, R. K.; Goodsell, D. S.; Olson, A. J. AutoDock4 and AutoDockTools4: automated docking with selective receptor flexibility. *J. Comput. Chem.* **2009**, *30*, 2785−2791.